

Compact Bright Radio-loud AGNs – III. A Large VLBA Survey at 43 GHz

X.-P. Cheng^{1,2,3}, T. An^{1,4}, S. Frey^{5,6}, X.-Y. Hong^{1,2,4}, X. He¹, K. I. Kellermann⁷, M. L. Lister⁸, B.-Q. Lao¹, X.-F. Li^{1,2}, P. Mohan¹, J. Yang^{1,9}, X.-C. Wu¹, Z.-L. Zhang¹, Y.-K. Zhang^{1,2}, W. Zhao^{1,4}

ABSTRACT

We present the observational results from the 43-GHz Very Long Baseline Array (VLBA) observations of 124 compact radio-loud active galactic nuclei (AGNs) that were conducted between 2014 November and 2016 May. The typical dimensions of the restoring beam in each image are about $0.5 \text{ mas} \times 0.2 \text{ mas}$. The highest resolution of 0.2 mas corresponds to a physical size of 0.02 pc for the lowest redshift source in the sample. The 43-GHz very long baseline interferometry (VLBI) images of 97 AGNs are presented for the first time. We study the source compactness on mas and sub-mas scales, and suggest that 95 sources in our sample are suitable for future space VLBI observations. By analyzing our data supplemented with other VLBA AGN surveys from literature, we find that the core brightness temperature increases with increasing frequency below a break frequency $\sim 7 \text{ GHz}$, and decreases between $\sim 7\text{--}240 \text{ GHz}$ but increases

¹Shanghai Astronomical Observatory, Chinese Academy of Sciences, Shanghai 200030, China; e-mail: antao@shao.ac.cn

²University of Chinese Academy of Sciences, 19A Yuquanlu, Beijing 100049, China

³Korea Astronomy and Space Science Institute, 776 Daedeok-daero, Yuseong-gu, Daejeon 34055, Korea

⁴Key Laboratory of Radio Astronomy, Chinese Academy of Sciences, 210008 Nanjing, China

⁵Konkoly Observatory, Research Centre for Astronomy and Earth Sciences, Konkoly Thege Miklós út 15-17, H-1121 Budapest, Hungary

⁶Institute of Physics, Eötvös Loránd University, Pázmány Péter sétány 1/A, H-1117 Budapest, Hungary

⁷National Radio Astronomy Observatory, 520 Edgemont Rd., Charlottesville, VA 22903, USA

⁸Department of Physics, Purdue University, 525 Northwestern Avenue, West Lafayette, IN 47907, U.S.A.

⁹Department of Earth and Space Sciences, Chalmers University of Technology, Onsala Space Observatory, SE-43992 Onsala, Sweden

again above 240 GHz in the rest frame of the sources. This indicates that the synchrotron opacity changes from optically thick to thin. We also find a strong statistical correlation between radio and γ -ray flux densities. Our correlation is tighter than those in literature derived from lower-frequency VLBI data, suggesting that the γ -ray emission is produced more co-spatially with the 43-GHz VLBA core emission. This correlation can also be extrapolated to the un-beamed AGN population, implying that a universal γ -ray production mechanism might be at work for all types of AGNs.

Subject headings: techniques: interferometric – galaxies: active – surveys – galaxies: jets – high angular resolution – (galaxies:) quasars: general

1. Introduction

Active galactic nuclei (AGNs) host the most powerful natural particle accelerators, producing also high-energy cosmic rays and neutrino emission. Compact jets emanating from around the central supermassive black holes (SMBHs) in radio-active AGNs are prominent sources in the widest range of electromagnetic wavebands, from radio wavelengths to γ -rays. AGN jets are in the forefront of modern multi-messenger astrophysical research (see [Blandford et al. 2019](#), for a recent review). Surveys of AGNs supply a wealth of information for advancing our understanding of jet physics. Of particular importance are high-resolution radio interferometric surveys that zoom directly into the parsec (pc) and sub-pc scale regions of AGN jets which are closely related to the extreme astrophysical phenomena.

Recently, the source of high-energy cosmic neutrinos (~ 300 TeV) detected by IceCube on 2017 September 22 was identified as a distant γ -ray blazar, TXS 0506+056, which is an intermediate synchrotron-peaked BL Lac object at a redshift of $z = 0.34$ ([Halzen et al. 2019](#); [IceCube Collaboration et al. 2018a,b](#)). This first confirmed that blazars are sources of high-energy astrophysical-origin neutrinos, opening a new window of studying the Universe using the unobstructed messenger neutrino ([IceCube Collaboration et al. 2018b](#)). It is widely speculated that high-energy cosmic rays are accelerated in the magnetic fields in the innermost jets of blazars. The generated cosmic rays interact with nearby gas, photons or other cosmic rays producing charged mesons that decay into high-energy neutrinos, γ -rays and other particles ([Reines 1960](#)).

Very long baseline interferometry (VLBI) is an elegant observing technique which provides the highest angular resolution. Blazars are among the most powerful objects in the Universe. Images from high-frequency high-resolution VLBI surveys of blazars are essential

to test jet models (e.g., Marscher 1995), and to investigate the innermost region of compact jets where the acceleration and collimation of the relativistic plasma flow takes place (Kellermann & Pauliny-Toth 1969; Gallimore et al. 2004; Lister et al. 2016) and where the high-energy neutrinos and γ -rays are produced (Ros et al. 2020).

The Large Area Telescope on-board the *Fermi* γ -ray space telescope (*Fermi*-LAT) has already detected 2683 AGNs, listed in the fourth *Fermi*-LAT catalog (Fermi-LAT collaboration 2019). Most of the sources are classified as blazars (comprising BL Lacs and optically violently variable quasars), which show prominent emission over a broad range of electromagnetic radiation, from radio to γ -ray energies. The spatial localization of the region where the γ -rays are emitted, γ -ray radiation mechanism in blazars, and correlation between radio and γ -rays are key questions to understand the blazar activity at multiple bands. Synchrotron radiation is responsible for the bump at radio to X-ray frequencies in the $\log \nu F_\nu$ versus $\log \nu$ spectral energy distribution (SED). Another dominant mechanism responsible for the bump from X-ray to TeV γ -ray regions is inverse-Compton (IC) radiation. Two possible scenarios are attributed to this: synchrotron self-Compton (SSC) radiation which results from IC scattering of synchrotron radiation by the same relativistic electrons that produced the synchrotron radiation, and external inverse-Compton (EC) radiation where the photons available for IC scattering in the inner jet are seeded from external sources such as the broad-line region (Sikora et al. 1994) and the accretion disk (Dermer & Schlickeiser 1993). One method to verify the process of SSC radiation is using the correlation between the mm-wavelength radio luminosity of the core and its γ -ray luminosity.

Some VLBI observations of blazars at high frequencies (e.g., Lee et al. 2008; Agudo et al. 2010; Piner et al. 2010) have revealed complex inner jet morphology and kinematics at sub-milliarcsecond (sub-mas) scales. New statistical studies show that the jets are accelerated in the sub-pc regions from the central engine (Lee et al. 2016). However, non-ballistic motion of the jet is found within a few parsec, e.g., NRAO 150 (Agudo et al. 2007) from observations with the Global mm-VLBI Array (GMVA) and the Very Long Baseline Array (VLBA) at 86 and 43 GHz, respectively. Thus, high-resolution VLBI observations and large complete surveys at high frequencies are important to study the jet structures and kinematics at sub-pc scales.

Ground-based VLBI observations show typical apparent core brightness temperature (T_b) in the range of $10^{11} - 10^{12}$ K (e.g., Moellenbrock et al. 1996). However, the Japanese VLBI Space Observatory Programme (VSOP, Hirabayashi et al. 1998) detected some AGNs with core brightness temperature higher than 10^{12} K (Tingay et al. 2001; Dodson et al. 2008). The highest brightness temperature that has been measured with VSOP is 5.8×10^{13} K for AO 0235+164 at 5 GHz (Frey et al. 2000). The maximum brightness temperature is deter-

mined by the longest baseline length, regardless of the observing frequency (Kovalev et al. 2005). The Russia-led *RadioAstron* mission (Kardashev et al. 2013) detected core brightness temperatures even higher than 10^{13} K (e.g., Kovalev et al. 2016; Pilipenko et al. 2018; Kutkin et al. 2018), about two orders of magnitude above the equipartition (Readhead 1994) and inverse Compton limits (Kellermann & Pauliny-Toth 1969). The interpretation of extremely high brightness temperatures is a challenge to AGN physics. Moreover, Lee et al. (2008) showed that the core brightness temperature will be small at lower frequencies due to opacity effect between 2 GHz and 15 GHz. However, their 86-GHz core brightness temperatures are significantly lower than those measured at 15 GHz. Therefore 43-GHz VLBI observations, straddling 15 and 86 GHz, are crucial to explore the maximum core brightness temperature and its corresponding frequency and to study core brightness temperature distribution along the jet which can be used to test models of the inner jet (Marscher 1995).

Despite more than 30 years of research of radio-loud AGNs at high frequencies with VLBI, only 163 sources were observed and imaged at 43 GHz (Lister 2001; Charlot et al. 2010; Jorstad et al. 2017; Cheng et al. 2018) and 263 AGNs have been successfully imaged at 86 GHz (Lee et al. 2008; Cheng et al. 2018; Nair et al. 2019). Most of these observations were carried out in snapshot mode, and high-quality images are scarce. Even fewer sources have multi-epoch imaging observations. In addition, the resolution is still not enough to explore the innermost jet emission region where the jet is formed and accelerated. Future space VLBI missions would leap forward in the direction of improving both the resolution and the imaging capability. A systematic survey of a large AGN sample is necessary to make progress of the future space VLBI proposals.

In this paper, we present the results of 43-GHz VLBA imaging of 124 AGNs and a statistical study of their compactness, core brightness temperatures, and the correlation between the radio and γ -ray emissions. The observations and the data reduction process are described in Sect. 2. We present the main results and comment on selected individual sources in Sect. 3. Section 4 contains the discussion of the properties of our sample, and a summary appears in Sect. 5. Throughout this paper, the standard Λ CDM cosmological model with $H_0 = 73 \text{ km s}^{-1} \text{ Mpc}^{-1}$, $\Omega_M = 0.27$, and $\Omega_\Lambda = 0.73$ is adopted.

2. VLBA Observations and Data Reduction

2.1. Sample Selection

As mentioned in Section 1, a large sample of compact and bright AGNs is important for the successful detection and imaging to support the scientific operation of ground-based

mm-wavelength and space VLBI. To enlarge and complete the existing database, we selected and observed 134 AGNs. The selection criteria are described in details in Paper I (An et al. 2014) and Paper II (Cheng et al. 2018). Ten bright AGNs were selected from our sample and observed at 43 and 86 GHz with long integration time and good (u, v) coverage, in order to further study the inner jet structures (Cheng et al. 2018). The remaining 124 sources consist of 97 quasars, 15 BL Lac objects, 6 radio galaxies, and 6 objects with no optical identification. We carried out an imaging survey at 43 GHz using the VLBA. Combined with the previous 43-GHz VLBI observations (Krichbaum & Witzel 1992; Lister 2001; Marscher et al. 2002; Lanyi et al. 2010), we obtain a large sample containing 260 AGNs to study brightness temperatures of AGN cores and to explore the jet acceleration mechanism. Table 1 lists general information of the sample: IAU source name (B1950.0), commonly used other source name, observation session, right ascension (RA), declination (Dec), redshift, optical classification, an indication of comments on the source in Sect. 3.3, and γ -ray photon flux (where available). The photon flux of the γ -ray bright AGNs are provided by the *Fermi*-LAT in the 100 MeV – 300 GeV energy range (Acero et al. 2015).

2.2. Observations

To ensure the success of the observations, we split the sources into two sub-samples, based on the source flux densities measured at lower radio frequencies. The first sub-sample consists of 40 bright sources for which we acquired good images, while the second sub-sample includes 84 relatively weaker sources which were observed less thoroughly. These sub-samples were observed in the corresponding sessions B and C, as listed in Column 3 of Table 1. Millimeter-wavelength VLBI observations are easily affected by tropospheric fluctuations, so the observing periods were carefully chosen to have exceptionally favorable weather conditions. The observations were spread over a period of almost one year from 2015 June to 2016 April as shown in Column 3 of Table 2 and in Column 2 of Table 3. Each of the 40 sources in session B was observed for four scans of 7 min duration. Each source in session C was observed for two 7-min scans separated by long time spans in order to obtain relatively uniform (u, v) coverage. Table 2 summarizes the observation setups. All ten VLBA antennas were used for the 43-GHz observations. At the beginning and the end of each observation, calibrator scans were scheduled on some of these bright quasars: 3C 84, 3C 273, 3C 279, 3C 345, 3C 454.3, 4C 39.25, 1749+096, or BL Lac.

The data were recorded with 2-bit sampling at an aggregate data rate of 2 Gbps, using 8 intermediate frequency (IF) channels of 32 MHz bandwidth each. The observations were made in both left and right circular polarizations. One scan on fringe finder sources every 1.5

h was used to check the recording, pointing, and calibration. Figure 1 shows a typical (u, v) coverage for sources observed in the first (session B) and second (session C) samples in the left and right panels, respectively. The raw VLBA data were correlated using the DiFX software correlator (Deller et al. 2007, 2011) at the Array Operations Center in Socorro (New Mexico, U.S.), with 2 s averaging time, 128 frequency channels per IF, and uniform weighting. The correlated data were transferred to computer clusters in the China SKA Regional Centre prototype (An, Wu, Hong 2019) where the calibration and imaging analysis were carried out.

2.3. Data Reduction

We processed the data in the standard way with the U.S. National Radio Astronomy Observatory (NRAO) Astronomical Imaging Processing Software (AIPS) package (Greisen 2003). First we loaded the data to AIPS by the task FITLD, and flagged the bad data points (typically due to inclement weather) before proceeding further. We selected Pie Town (PT) as the reference antenna for most of the data. Fort Davis (FD) was used as the alternative reference telescope. In the amplitude calibration, we first removed the sampler bias with the task ACCOR, then calibrated the correlator output with APCAL and fitted for the ionospheric opacity correction using weather information, antenna system temperature and gain curve tables. Then we fringe-fitted a short (generally 1 min) scan of calibrator source data to determine the phase and single-band delay offsets and applied the solutions to the calibration table. After removing instrumental phase offsets from each IF, we performed a global fringe-fit using the task FRING by combining all IFs to determine the frequency- and time-dependent phase corrections for each antenna and removed them from the data. To avoid false detections, fringe-fitting was done with a minimum signal-to-noise ratio (SNR) of 5. After fringe-fitting, the solutions for the sources were applied to their own data by linear phase connection using rates to resolve phase ambiguities. In the final step, we used the task BPASS to calibrate the bandpass shapes by fitting a short data scan on a calibrator, and applied the solutions to all data. Then we made single-source calibrated data sets with SPLAT/SPLIT and used the task FITTP to export the calibrated visibility data files to the external work space in the clusters. These single source data files were then imported in the DIFMAP program (Shepherd 1997) to carry out self-calibration and imaging. A few runs of phase-only self-calibration were made to eliminate the residual phase errors. Amplitude self-calibration was performed with the amplitude normalization when the CLEAN models reached an integrated flux density close to the correlated amplitude on the shortest baselines. The determined overall telescope gain correction factors were found to be small, typically within 10%, in agreement with other similar 43- and 86-GHz VLBA surveys (Jorstad et al.

2017; Nair et al. 2019).

2.4. Model Fitting

We used a number of circular Gaussian components to model the brightness distribution structure of each source in the visibility domain in DIFMAP. Typically 1 to 6 components were used to represent the detected features of the source structure. The radio core is identified as the bright and compact component at the apparent jet base. The fitted parameters are cataloged in Table 4. The sizes of these compact jet components are usually smaller than the synthesized beam. The minimum resolvable size of a component in a VLBI observation is given by Lobanov (2005):

$$d_{\text{lim}} = \frac{2^{1+\beta/2}}{\pi} [\pi B_{\text{maj}} B_{\text{min}} \ln 2 \ln \frac{(S/N)}{(S/N) - 1}]^{1/2}, \quad (1)$$

where B_{maj} and B_{min} are the major and minor axes of the restoring beam, respectively (full width at half-maximum, FWHM), S/N is the signal-to-noise ratio, and β is the weighting function, which is 0 for natural weighting or 2 for uniform weighting. We took d_{lim} as the upper limit for the components with the fitted size $d < d_{\text{lim}}$.

3. Results

3.1. VLBA Images

Figure 2 shows contour plots of the final naturally weighted total intensity images for all the 124 sources. For 97 sources, the survey provides the first-ever VLBI image made at 43 GHz, extending the existing database by about 60%. Most of the sources shown here have secondary features or have complex structures. For these objects, we give brief comments on the characteristics of the radio structure, comparing our observations with other lower-frequency VLBI observations from the literature as discussed in the next subsection. The typical image size is 3 mas \times 3 mas and the dimensions of the restoring beam in each image are 0.5 mas \times 0.2 mas. The elliptical Gaussian restoring beam size is indicated in the bottom left corner of the maps in Fig. 2. The peak intensity and the rms noise level are given in the bottom right corner of the maps. The lowest contour represents 3 times the off-source image noise level, and the contours are drawn at $-1, 1, 2, 4, \dots, 2^n$ times the lowest level. Table 3 provides the parameters relevant to the images: source name, observation date, beam size, integrated flux density, peak intensity, off-source rms noise in the CLEAN image, correlated

flux density on the shortest baselines, the length of the shortest baseline, correlated flux density on the longest baselines, and the length of the longest baseline.

Among the most important parameters derived from high-frequency VLBI surveys are the source compactness and core brightness temperature. Blazars often shows a one-sided core–jet structure, and the core is usually the most compact and bright component at one end of the jet. Eight other sources in our sample are identified as compact symmetric objects (CSOs, An, & Baan 2012) or gigahertz-peaked spectrum (GPS, Stanghellini et al. 1998) sources: 0738+313, 0742+103, 0743–006, 1435+638, 2021+614, 2126–158, 2134+004, and 2209+236. All these sources, except 2021+614, are GPS sources, which show a sharp low-frequency spectral cutoff near 1 GHz. The exceptional source 2021+614 is a well-known CSO (Polatidis & Conway 2003), but we are unable to identify the core component from our image. Comments on selected sources, including the designation of the core we used for calculating the core brightness temperature and the reliability of faint features in the images are given in Sec. 3.3. Table 4 lists the model-fitting parameters: source name, observation epoch, component identifier, model flux density, peak intensity, angular separation from the core, size of the components, position angle of the components.

3.2. Parsec-scale Morphology

The sources in our sample can be divided into four basic classes based on their morphology: simple core, one-sided core–jet, compact symmetric object, and complex structure. Eight sources (0847–120, 1049+215, 1257+519, 1329–049, 1417+385, 1657–261, 2325+093, 2342–161) have a single core component. One hundred and twelve sources show a core and a one-sided jet structure. However, 8 sources (0113–118, 0221+067, 0708+506, 0736+017, 0805–077, 1124–186, 1219+044, 2227–088) have faint extended radio emission and for 5 sources the cores (0605–085, 1036+054, 1045–188, 2021+317, 2223+210) are not the brightest but the most compact among the fitted components. Three sources (0241+622, 0743–006, 2021+614) show compact symmetric jet structure. We detect a component exceeding 7σ noise level in the counter-jet direction in 0241+622. 0743–006 is GPS source that shows a triple structure. 2021+614 is a well-known CSO, showing two-sided structure. One source (0354+559) shows a complex structure, as shown in Sect. 3.3.

Given our selection criteria, all sources have VLBI images at lower frequencies, at least at 2.3 and 8.4 GHz. Almost all sources also have radio images in literature showing their kpc-scale structure based on Very Large Array (VLA) observations. By comparing the radio structures from pc to kpc scales, we find that there are 6 sources showing completely oppositely-directed jet structures on mas and arcsec scales, and 23 sources display a relatively

large change in the apparent jet direction.

3.3. Comments on Selected Individual Sources

0048–071 (OB –082): Our 43-GHz image shows a single-sided jet to the northwest, in an opposite direction of the kpc-scale lobe (Kharb et al., in prep.)¹.

0106+013 (4C +01.02): Our image shows that the innermost jet structure (< 1 mas) is along the east–west direction (in a position angle $\sim -110^\circ$), then it bends towards the southwest ($\sim -140^\circ$) at about 2 mas from the core. This is in agreement with the low-frequency VLBI images (Lister et al. 2009).

0113–118: This source is very compact at 43 GHz, we only detect a core and a faint extension within 1 mas. However, it was not detected on space–ground baselines in the 5-GHz VSOP AGN Survey (Dodson et al. 2008).

0119+041 (OC +033): The brightness temperature of the core is 1.6×10^{10} K at 43 GHz, the derived Doppler factor is below unity which is consistent with slow jet motion found in the literature (Lister et al. 2009; Piner et al. 2012). Neither the *Compton* Gamma Ray Observatory Energetic Gamma Ray Experiment Telescope (EGRET) nor *Fermi*/LAT has detected this source. The 15-GHz light curve from the Owens Valley Radio Observatory (OVRO) 40-m radio telescope shows that the flux density does not have significant variation from 2008 to mid-2017 (Richards et al. 2011). The VLBI structure (the core and the eastern jet component) does not show noticeable change (Lister et al. 2009; Piner et al. 2012). The overall radio spectrum peaks at about 7 GHz. All these pieces of evidence imply that this is a GPS source, rather than a blazar.

0122–003 (UM 321): Our image shows a compact core and three jet components along a straight line to the west. It is in good agreement with the 5- and 15-GHz VLBA images (Fomalont et al. 2000; Lister et al. 2013).

0130–171 (OC –150): The compact core is 0.08 mas in size. We detected a series of jet components extending to the southwest.

0149+218: This source shows a compact structure at 43 GHz. A relatively weak component extending to the north is detected.

0202–172: The jet shows a centrally symmetric S-shaped morphology within 5 mas. An

¹<http://www.physics.purdue.edu/astro/MOJAVE/sourcepages/0048-071.shtml>

extended feature is located at ~ 2 mas from the core, sitting in the gap between the inner jet and the outer 3 mas jet.

0208+106 : The jet points to southeast up to 1 mas from the core, then it bends towards northeast seen in the 15-GHz VLBA image obtained in the Monitoring Of Jets in Active galactic nuclei with VLBA Experiments (MOJAVE) survey (Lister et al. 2009), with a 70° change in position angle. The outer (> 1 mas) bent jet is diffuse at 43 GHz.

0221+067 (4C +06.11): The source shows a compact core–jet structure within 1 mas. Our high dynamic range image detected two weaker jet components to the west.

0224+671 (4C +67.05): The core is 0.13 mas in size. A jet component to the north is detected and has the similar flux density with the core at 43 GHz.

0229+131 (4C +13.14): The source displays considerable emission on both sides of the core at arcsec scales (Punsly 1995). Our image shows a bright core and an inner jet pointing to the northeast which is consistent with the high-resolution 5-GHz VSOP image (Dodson et al. 2008).

0239+108 (OD +166): It shows a compact core–jet structure. According to the total flux density light curve from the 15-GHz OVRO monitoring program (Richards et al. 2011), our 43-GHz observation was made in a fading phase of the source.

0241+622 : This is a low-redshift ($z = 0.045$) Seyfert 1.2 galaxy (Véron-Cetty & Véron 2006). The eastern jet component is consistent with the 15-GHz VLBA image (Lister et al. 2009). However, there is another component appearing on the opposite (western) side of the core with an intensity in excess of 7σ image noise, indicating a reliable detection. A detailed study of this component would require future high-resolution and high-sensitivity VLBI observations.

0306+102 (OE +110): The source is very compact in lower-frequency VLBI images. A faint radio emission is detected in the northeast.

0309+411 (NRAO 128): This is a strongly core-dominated broad-line radio galaxy showing core and double lobes morphology (de Bruyn 1989; Marcha et al. 1996). Our 43 GHz VLBA image reveals a prominent core and a straight jet extending to 1 mas, aligning with the brighter and advancing kpc-scale jet.

0354+559: The source shows a complex jet in low-frequency VLBI images (Fomalont et al. 2003). In our 43-GHz image, the jet points to the northwest and then bends to the southwest within 1 mas. The source has rich structure even at mas and probably sub-mas scale, calling for a detailed study.

0400+258 (CTD 026): The core size is 0.21 mas. The jet extends to the southeast up to about 2 mas; this is also seen by [Dodson et al. \(2008\)](#). Further out, the jet becomes diffuse and bends to northeast, as seen only at larger scales with lower-frequency VLBI imaging (e.g., [Fomalont et al. 2000](#); [Lister et al. 2009](#)).

0403–132 (OF –105): Our 43-GHz VLBA image shows a very compact core and faint jet emission extending to the southeast. [Cooper et al. \(2007\)](#) detected an unresolved core and radio emission to the southwest. The VLBI data at 2.3 and 15 GHz exhibit a bright core and jet emission extending to the southern direction ([Fomalont et al. 2000](#); [Lister et al. 2009](#)).

0405–123 (OF –109): This source is the second Seyfert 1.2 galaxy in our sample ([Véron-Cetty & Véron 2006](#)). The VLA image shows two hot spots in the north–south direction, and only the one in the northern lobe was detected in X-rays and optical ([Sambruna et al. 2004](#)). The lower-frequency VLBI images show a core–jet structure extending ~ 30 mas to the north. Our image shows a resolved structure within 2 mas, with the south component corresponding to the core.

0507+179: [de Vries et al. \(2000\)](#) identified it as a BL Lac object. The core brightness temperature is the maximum in our sample.

0529+075 (OG 050): Our image shows the inner jet extending to the northwest within 3 mas. However, the kpc-scale structure is pointing to the opposite direction ([Cooper et al. 2007](#)).

0605–085 (OC –010): The most important concern for this source is the core identification, considering that our observation took place during a flare ([Richards et al. 2011](#)). Two components along the east–west direction have equal brightness. Referring to the 15-GHz VLBA image ([Lister et al. 2009](#)), we assume that the most compact and upstream component, i.e., the western component, is the core, even if it is not the brightest one. Further high-frequency VLBI observations are needed to confirm this.

0648–165: The source shows a large jet bending from the northwest as indicated by our image to the west-southwest which can be better seen in lower-frequency VLBI images ([Lister et al. 2009](#); [Pushkarev & Kovalev 2012](#))

0657+172: The jet direction of the source at pc scale in our image (west-northwest) is different from that seen in low-frequency (2.3- and 8.6-GHz) VLBI images ([Pushkarev & Kovalev 2012](#)). Based also on radio spectrum data², we suggest this source is a GPS or

²NASA/IPAC Extragalactic Database, <http://ned.ipac.caltech.edu/>

high-frequency peaker (HFP) candidate.

0723–008: Our image shows a jet pointing to the northeast at $\sim 35^\circ$ position angle, in a good agreement with the 15-GHz VLBA image (Lister et al. 2009).

0736+017 (OI +061): We only detect a compact core and a new weak jet component to the northeast at a distance of 0.41 mas.

0738+313 (OI +363): This is a GPS quasar (Stanghellini et al. 1998). Our 43-GHz VLBA image shows a core–jet structure, consistently with the 15 GHz-image (Stanghellini et al. 2001). Although the position of the radio core in this AGN is uncertain, we assumed the most compact feature at the base of the jet as the core. A more extended component appears at 3.5 mas south of the core.

0742+103 (OI +171): This is a high-redshift ($z = 2.624$) GPS quasar (Stanghellini et al. 1998) which shows a large jet bending. We detect a bright component and two diffuse inner jet components in the northwest within 3 mas at 43 GHz. Further out, the jet bends to the northeast in the 15-GHz VLBA image (Lister et al. 2009). The 1.4-GHz³ and 2.3-GHz (Pushkarev & Kovalev 2012) VLBA images show the jet bending from northeast to southeast. Although the position of the radio core in this GPS source is uncertain, we assumed the most compact feature at the base of the jet as the core. The coherent jet bending from northwest (inner ~ 2 mas) to northeast (inner 4 mas), to east (12 mas), then to southeast (~ 200 mas) suggests a 180° curved trajectory.

0743–006 (OI –072): This is a GPS quasar (Stanghellini et al. 1998). Although the core position is uncertain, we assumed the most compact feature at the base of the jet as the core.

0838+133 (3C 207): This is a powerful Fanaroff–Riley II (FR II) radio galaxy (Laing et al. 1983). The 1.4- and 8.4-GHz VLA images show a fairly symmetric triple structure (Bogers et al. 1994). Our 43-GHz VLBA image shows a bright core and a one-sided extended jet towards the east. This is in good agreement with what was found previously at 1.4 and 15 GHz (Lister et al. 2009).

0859–140 (OJ –199): The source shows a compact core and two lobes aligned in the north–south direction at 408 MHz (Bondi et al. 1996). Our image shows a faint and smoothly curved jet to the south-southeast within 2 mas, which is in good agreement with the previous

³Here and elsewhere, when we refer to 1.4-GHz VLBA images, we used the unpublished data observed in the project BG196 (PI: D. Gabuzda); calibrated data were downloaded from the Astrogeno database (<http://astrogeo.org/>).

15-GHz VLBA image (Kellermann et al. 1998).

0906+015 (4C +01.24): The VLA image at 1.6 GHz shows a compact core and a bright component 12'' east of the core on kpc scale (Murphy et al. 1993). The 2.3-, 8.6-, and 15-GHz VLBI images show a jet toward the northeast from 5 to 30 mas (Fey & Charlot 2000; Lister et al. 2009). There are 3 jet components detected towards the northeast within 2 mas in our 43-GHz image.

0945+408 (4C +40.24): The large-scale structure of this source is resolved into a very compact core with a one-sided jet extending over 4'' (~ 18 kpc) in the northeast direction using the VLA at 5 GHz and the Multi-Element Radio-Linked Interferometer Network (MERLIN) at 408 and 1666 MHz (Reid et al. 1995). The inner jet structure extends to southeast in our image, which appears to have a 90° misalignment with respect to the large-scale structure.

1036+054: The 1.4-GHz VLA image shows a bright core and extended jet emission structure in the northeast–southwest direction until $\sim 18''$ (Kharb et al. 2010). The 1.4-GHz VLBA image detected a one-sided jet pointing to the northeast over ~ 150 mas. The position of the 15-GHz core (Lister et al. 2009) coincides with the southernmost component in our image. The brightening jet component might be associated with the major outburst in late 2014 seen in the OVRO 40m light curve (Richards et al. 2011). Taking into account of the jet proper motion of 0.22 mas yr^{-1} (Lister et al. 2019) and the time interval between the outburst and our VLBA observation (2015 October 10), the flare-generated shock should have moved about 0.4 mas downstream, roughly consistently with the bright jet component seen in our 43-GHz image.

1045–188 (OL –176): The 1.4-GHz VLA image shows a bright core and extended jet emission structure in the northwest–southeast direction until $\sim 14''$ (Kharb et al. 2010). The 1.4-GHz VLBA image shows a one-sided jet pointing to the northeast over ~ 55 mas. The typical beam size at 15 GHz in the MOJAVE survey is $1.5 \text{ mas} \times 0.5 \text{ mas}$ (Lister et al. 2009). In our new 43-GHz image, we detected two components within the area of the 15-GHz beam. We assumed the most compact and northernmost component as the core. Our J1 component corresponds to the bright 15-GHz core. More high-frequency VLBI observations are needed to clarify this.

1124–186 (OM –148): Fey et al. (2015) only detect a compact core at 2.3 and 8.6 GHz. We detect a core and an extended faint emission feature to the south, in agreement with the 15-GHz image (Lister et al. 2009).

1150+497 (4C +49.22): The 1.5-GHz VLA image shows a complex triple source with a halo in the north–south direction (Ulvestad et al. 1981). The source is not detected on

space–Earth baselines at 5 GHz with the VSOP (Dodson et al. 2008). In our image, we detect a bright core and a series of jet components to the southwest.

1219+044 (4C +04.42): The source shows a compact core and extended jet emission aligned in the north–south direction until $\sim 5''$ (Kharb et al. 2010). The 15-GHz VLBA image only detected a one-sided jet pointing to the south until 7 mas (Lister et al. 2009). Our new image shows a bright core and a faint emission to the south.

1228+126 (M87): This is a well-known low-luminosity FR I radio galaxy (Laing et al. 1983). The large-scale image of M87 observed with the VLA at 90 cm wavelength suggests that the outward flow from the nucleus extends well beyond the 2 kpc radio jet (Owen et al. 2000). The 15-GHz VLBA image displays an unresolved core and complex jet structure with an extent of 22 mas. Our 43-GHz VLBA image suggests a limb-brightening morphology with two ridge lines extending to the northwest and west directions. The jet opening angle, estimated from the northern and southern bright jet knots, is about 45° in projection, as is approximately consistent with the value reported in Hada et al. (2016) and Zhao et al. (2019).

1324+224: The deep VLA image at 1.4 GHz only detected a compact core (Cooper et al. 2007). The 1.4-GHz VLBA image shows the jet pointing to the northwest up to 10 mas, then bending towards northeast until 90 mas from the core. In the 15-GHz VLBA image, the source shows a very compact core and a weak emission feature approximately 3 mas to the southwest (Lister et al. 2009). However, our new 43-GHz image indicates an inner jet towards the northwest on an angular scale of 2 mas, at a position angle consistent with the 1.4-GHz VLBA image.

1435+638 (VIPS 0792): The 1.4-GHz VLA image presents a faint lobe separated from the core by $15.4''$ in the southwest. It was not detected at 5 GHz (Reid et al. 1995). Previous studies presumed the radio core to lie at the northernmost end of the jet, based on the 5-GHz and 15-GHz VLBA maps (Helmboldt et al. 2007; Lister et al. 2016). We also associated the northeastern component with the radio core in our image.

1504–166 (OR –107): The 1.4-GHz VLA map exhibits only radio core emission (Kharb et al. 2010). The 1.4-GHz VLBA image shows the jet pointing to the west up to ~ 150 mas. The 8- and 15-GHz VLBI images show a compact core and extended structure to the south and southeast (Lister et al. 2009; Pushkarev & Kovalev 2012). Our new 43-GHz image shows the inner jet pointing to the south which suggests a jet bending.

1514+004 (4C +00.56): The source is a nearby radio galaxy ($z = 0.052$). The 1.4-GHz NRAO VLA Sky Survey (NVSS) image shows a symmetric triple source extending in the northwest–southeast direction (Condon et al. 1998). In our image, we detect a core and

bright jet component pointing to the northwest, in good agreement with the 15-GHz VLBA image (Lister et al. 2009).

1548+056 (4C +05.64): Kharb et al. (2010) detected a bright core and a relatively faint extended radio emission to the north with the VLA at 1.5 GHz. On mas scales, the source is dominated by a compact core with a jet extending to the north, as was seen previously at 1.4 GHz. In our image, we see a complex and curved jet extending to north and then bending to the northeast at 2 mas from the core.

1637+826 (NGC 6251): This is a well-studied FR I radio galaxy which shows both a bright core and large extended asymmetric jet emission (Perley et al. 1984). Lower-frequency VLBI observations only detected the jet extending to the southwest direction (Fey et al. 2004; Lister et al. 2009). Our 43-GHz image shows the jet aligned well with the kpc-scale jet.

1716+686: The 4.5-GHz VLA observation shows a diffuse halo of $10''$ extension surrounding the core (Taylor et al. 1996). Lister et al. (2009) presented a jet extending to the northwest up to ~ 10 mas, in a position angle in agreement with our image within 2 mas.

1926+611: The 1.5-GHz VLA image only detected a core (Condon et al. 1998), but the 1.7-GHz VLBI image shows a bright core and a jet structure extended to the south (Polatidis et al. 1995). However, our image exhibits two jet components to the southeast, in agreement with the 15-GHz VLBA image (Lister et al. 2009). This indicates a jet bending from the south to the southeast, with nearly 70° change in the position angle.

2007+777: The image made with the VLA at 1.5 GHz shows two-sided radio emission in the east–west direction (Antonucci et al. 1986). The eastern component is a prominent hot spot (Murphy et al. 1993). Our image shows the jet extending to the west, corresponding to the western side of the jet in the VLA image.

2021+317 (4C +31.56): The 1.4- and 15-GHz VLBA images display the jet extending towards the south (Lister et al. 2009), consistently with our new 43-GHz VLBA image. However, we also detect a new component off-axis from the persistent jet, on the northwestern side. We believe this northwestern component is the core, and therefore the jet undergoes a sudden bending within 1 mas. Future observations can confirm the properties of this intriguing object.

2021+614 (OW +637): The source was classified as a CSO (Tschager et al. 2000). No radio emission was detected on scales larger than $0.2''$ with the VLA at 1.4 GHz (Kharb et al. 2010). Lister et al. (2009) identified the core feature located in the end of the southwestern component. We also use the same component as the core for our image, even though the J3 component at ~ 2.5 mas is more compact than the core.

2029+121 (OW +149): The image made with the VLA in A-array at 1.4 GHz shows a one-sided, edge-brightened morphology pointing to the northwest (Rector & Stocke 2001). The jet in our image extends to the southwest in -130° position angle, in agreement with the 2.3- and 8.6-GHz VLBA images (Fey et al. 2015).

2126–158 (OX –146): This is the highest-redshift AGN in our sample ($z = 3.268$), a GPS quasar (Stanghellini et al. 1997). The peak emission component in our image has a flat spectrum between 5 and 15 GHz and is also identified as the core by Stanghellini et al. (2001). Our image shows a bright core and a faint jet extending to the southwest.

2134+004 (OX +057): Tornaiainen et al. (2005) identified this source as a GPS quasar. Orienti et al. (2006) found that the core of the source is located in the easternmost component. The core is also the brightest component in the 43-GHz radio structure.

2141+175 (OX +169): Large-scale VLA observations only detected a core at 1.4 GHz Condon et al. (1998). In the 2.3- and 8.6-GHz VLBI images, the jet extends to the north, out to a distance of 25 mas (~ 85 pc) (Petrov et al. 2005). We detect the jet initially pointing to the west and then changing its position angle to the northwest, indicating that it has a large ($\sim 90^\circ$) bending that starts at ~ 0.2 mas.

2155–152 (OX –192): The image made with the VLA at 1.4 GHz shows a triple structure with a size of $6''$ surrounding a central compact component in the north–south direction (Cooper et al. 2007). Our image shows a jet towards the southwest up to 2 mas, in good agreement with the 5- and 15-GHz VLBA images (Fomalont et al. 2000; Lister et al. 2009).

2209+236: Dallacasa et al. (2000) identified the source as a HFP. The 5-GHz VLBA image (Fomalont et al. 2000) shows no indication of extended emission. Lister et al. (2016) found a jet component to the northeast and determined a maximum apparent proper motion $1.35c$. Our image shows the inner jet bending to the northeast.

2223+210 (DA 580): The jet structure extends to southwest in the 2.3-, 8.6-, and 15-GHz VLBI images (Beasley et al. 2002; Lister et al. 2009). We detect two compact components inside the low-frequency VLBI core region. Although the eastern one is not the brightest component, it appears in the upstream direction. Therefore we identify this as the radio core.

2227–088: The source shows an integrated flux density of 2.7 Jy in the core at 43 GHz, and only 21 mJy in the extended emission. Tingay et al. (2003) found this source highly variable at 4.8 GHz with Australia Telescope Compact Array (ATCA). The many VLBI

images made at lower frequencies⁴ indicate a faint, wiggling jet towards the north.

2234+282 (CTD 135): [Lister et al. \(2016\)](#) identified the core in this BL Lac object with the northernmost jet feature in their 15-GHz VLBA images. Earlier [An et al. \(2016\)](#) claimed this source to be a rare γ -ray emitting CSO candidate with a two-sided jet, based on a comparison of VLBA maps at 8.4 and 15 GHz. In our new 43-GHz image, the southwestern component is the brightest and most compact, suggesting that this is the true core, instead of the northeastern feature ([Lister et al. 2016](#)). Also, our new observations are at odds with the CSO interpretation ([An et al. 2016](#)).

2243–123: The jet points to the northeast in the previous 5- and 15-GHz VLBA images ([Fomalont et al. 2000](#); [Lister et al. 2009](#)). In our image, the innermost section of the jet points closer to the north, within 4 mas from the core.

2318+049 (OZ +031): VLA images show a barely resolved structure along -40° position angle ([Hutchings et al. 1998](#)). In our VLBA image, the source shows a compact core–jet structure extending to the northwest in about the same direction. This is consistent with lower-frequency VLBI images (e.g., [Fomalont et al. 2000](#); [Lister et al. 2009](#)). Note that the 5-GHz VSOP Survey image also shows emission within 2 mas extended in the same direction, albeit with no clear indication of the core ([Scott et al. 2004](#)).

4. Discussion

4.1. Source Compactness

Only sources with cores that are compact enough can be successfully detected with the high angular resolution provided by high radio frequency VLBI observations. The source compactness is often expressed in two ways: the ratio of the VLBI core flux density to the total flux density, or alternatively, the ratio of the correlated flux density on the longest baselines to that on the shortest baselines ([Lee et al. 2008](#); [Kovalev et al. 2005](#); [Cheng et al. 2018](#)). Figure 13 shows the distributions of the total flux density S_{tot} , the ratio $S_{\text{core}}/S_{\text{tot}}$, the correlated flux density on longest baselines derived from our data S_{L} , and the ratio $S_{\text{L}}/S_{\text{S}}$, using the values listed in Table 3. S_{core} is obtained from fitting the brightest core component with a circular Gaussian model in DIFMAP (see Table 4). S_{tot} is estimated by integrating the flux density contained in the emission region in the VLBI image. S_{L} and S_{S} are obtained from the correlated flux density on the longest and shortest baselines. The total flux density

⁴see <http://astrogeo.org/>

of these sources S_{tot} (Fig. 13a) ranges from 0.10 to 2.91 Jy. The correlated flux density on the longest baselines S_{L} (Fig. 13c) ranges from 0.02 to 2.38 Jy. The median values of the flux densities S_{tot} and S_{L} in our sample are 0.63 Jy and 0.26 Jy, respectively.

Figure 13b gives the distribution of $S_{\text{core}}/S_{\text{tot}}$. Since most cores are even unresolved at 43 GHz with $0.5 \text{ mas} \times 0.2 \text{ mas}$ resolution, the ratio $S_{\text{core}}/S_{\text{tot}}$ denotes the source compactness on mas scales, which varies in the range of 0.21–1.0 with a mean value of 0.85. This is also a measure of the core dominance in the VLBI image. For 112 sources (accounting for 90% of the sample), the compactness parameter $S_{\text{core}}/S_{\text{tot}}$ is larger than 0.5, indicating that a substantial fraction of the 43-GHz VLBI emission is from the core. There are 96 sources with a core flux density exceeding 0.30 Jy (Fig. 13a). Figure 13d gives the distribution of the source compactness $S_{\text{L}}/S_{\text{S}}$, ranging from 0.08 to 0.99 with a mean value of 0.65. The visibility amplitude on the longest baseline is associated with the most compact and unresolved part of the core, therefore it is used as an indicator of the compactness on sub-mas scales. A total of 86 sources have $S_{\text{L}}/S_{\text{S}} > 0.5$. In general, the ratios $S_{\text{core}}/S_{\text{tot}}$ are higher than $S_{\text{L}}/S_{\text{S}}$, consistent with the observational results that some cores are further resolved at higher sub-mas resolutions.

The source compactness parameters are useful for planning mm-wavelength ground-based and/or space VLBI observations. For the proposed Chinese SMVA project (Hong et al. 2014), the expected highest angular resolution will be $20 \mu\text{as}$ at 43 GHz, and the baseline sensitivity is $\sim 17 \text{ mJy}$ (1σ , assuming 512 MHz bandwidth, 60 s integration) when a space-borne 10-m radio telescope works in tandem with a 25-m VLBA telescope. To explore the innermost jets using space VLBI at even higher resolution, the extremely compact AGNs would be the preferred targets. However, some of the objects in this sample do not contain a bright, compact component and thus are not suitable for imaging with the future space VLBI network. Based on the flux densities and model-fitting results in Table 3, 95 sources have $S_{\text{L}} > 0.17 \text{ Jy}$ (i.e. about 10 times the baseline sensitivity of the SMVA), $S_{\text{core}}/S_{\text{tot}} > 0.5$ and $S_{\text{tot}} > 0.30 \text{ Jy}$. These sources remain compact at the longest available ground-based baselines and have sufficiently high flux densities. Therefore, combined with the previous 10 sources in paper II (Cheng et al. 2018), there are 105 sources suitable for future space VLBI missions (Kardashev 2017; An et al. 2020).

4.2. Core Brightness Temperature

We estimated the brightness temperature of the core components, and listed the values in Column 9 of Table 4. We used the results of our brightness distribution model fitting,

and the following formula:

$$T_b = 1.22 \times 10^{12} \frac{S}{\nu^2 d^2} (1 + z), \quad (2)$$

where S is the flux density of the core in Jy, z is the redshift, ν is the observing frequency in GHz, and d is the fitted Gaussian size (FWHM) of the component in mas.

The median value of the core brightness temperatures (Table 4) is 7.92×10^{10} K, with a maximum of 2.54×10^{12} K. The maximum value is higher than the equipartition T_b limit (Readhead 1994; Begelman et al. 1994) but is approximately equal to the maximum brightness temperature set by the inverse Compton limit (Kellermann & Pauliny-Toth 1969). Apparent brightness temperatures exceeding the equipartition value are probably due to Doppler boosting of the relativistically beamed jet but could also be due to an intrinsic excess of particle energy over magnetic energy (e.g., Kardashev 2000; Kellermann 2002).

Figure 14a shows the observed brightness temperatures (T_b) as a function of frequency in the rest frame of source, $\nu = \nu_{\text{obs}}(1 + z)$. We adopted VLBI core brightness temperatures measured at observing frequencies ν_{obs} at 2, 5, 8, 15, and 22 GHz from the literature (Moellenbrock et al. 1996; Horiuchi et al. 2004; Kovalev et al. 2005; Pushkarev & Kovalev 2012), at 43 GHz (present data and Paper II), and at 86 GHz (Lee et al. 2008; Cheng et al. 2018; Nair et al. 2019), to study the relation between brightness temperature and frequency. From Fig. 14a, it is obvious that the core brightness temperatures at 43 and 86 GHz are much lower than those at 2, 5, 8, 15, and 22 GHz. The T_b values at lower frequencies, although with large scatter, seem to change only slightly with increasing frequency, until about 20 GHz. After that, a remarkable drop of T_b is seen above ~ 30 GHz. In order to quantify the variation of the core brightness temperature, we divided all 889 data points into 30 frequency bins, each containing 28–30 data points. Figure 14b shows the data averaged within the bins with the error bars representing the scatter. The horizontal error bars indicate the frequency range within the bin, and the vertical error bars show the standard deviation of the mean values of core brightness temperature. The T_b distribution can be fitted with a smoothly broken power-law function between 2–240 GHz (eq. 3), while the T_b values between 240–420 GHz (red-colored data points) seem to deviate from this relation and thus are excluded from the fitting:

$$T_b(\nu) = T_{b,j} \left[\left(\frac{\nu}{\nu_j} \right)^{\alpha_1 n} + \left(\frac{\nu}{\nu_j} \right)^{\alpha_2 n} \right]^{-1/n}, \quad (3)$$

where $T_{b,j}$ is the observed brightness temperature at the break frequency ν_j , $-\alpha_1$ and $-\alpha_2$ are the slopes at higher and lower frequencies than the break frequency, respectively, and n is a numerical factor controlling the sharpness of the break. The frequencies (horizontal axis) have been corrected to the source rest frame by multiplying the observing frequencies by $(1 + z)$. We choose the numerical factor $n = 1.97$ and use the nonlinear least-squares

algorithm to fit the function. Figure 14b shows the best fit with the following parameters: $T_{b,j} = (218.14 \pm 5.27) \times 10^{10}$ K, $\nu_j = 6.78 \pm 0.43$ GHz, $\alpha_1 = 1.91 \pm 0.03$, and $\alpha_2 = -0.94 \pm 0.06$.

From the best fitting parameters, we find that the core brightness temperature is increasing below the break frequency ~ 7 GHz, and decreasing between 7–240 GHz. $T_{b,j}$ is $\sim 2 \times 10^{12}$ K at ~ 7 GHz, which is slightly higher than the inverse Compton catastrophe limit (Kellermann & Pauliny-Toth 1969) and significantly higher than the equipartition value (Readhead 1994; Begelman et al. 1994), consistent with Doppler boosting in AGN jets. The inferred broken power-law distribution can be explained in terms of opacity affecting the emission mechanism at different resolutions. Below 7 GHz, due to relatively lower resolutions, the core emission is mixed with jet emission, resulting in lower T_b at lower frequencies. From 2 to 7 GHz, with the resolution increasing, this dilution effect gradually becomes weaker, thus the T_b shows an increasing trend. The decreasing trend of T_b starting from 7 GHz to higher frequencies reflects the synchrotron opacity changing from optically thick to thin. A resulting lower brightness temperature has been found by opacity core-shift observations in many sources (Kovalev et al. 2008; O’Sullivan & Gabuzda 2009; Sokolovsky et al. 2011). Previous compactness studies suggest that most, if not all, AGN cores are resolved into sub-components at higher frequency and with higher resolution. However, the highest-frequency data (red-colored data point) in our Fig. 14b show a clear deviation from the fitted trend (black line) and display a flattening. The inferred brightness temperatures are substantially higher than the values expected from the fit. We caution that this may be because of the sample selection bias caused by the flux density limited surveys. These high-frequency (> 240 GHz in rest frame) data correspond to high-redshift ($z \gtrsim 3$) AGNs. Among those, the survey samples include the few brightest ones only, and the majority of the (much weaker) high-redshift population is missed. Future higher-sensitivity VLBI surveys at and above 86 GHz containing weaker high-redshift AGNs would be important for identifying the distribution trend at the very high frequency end of Fig. 14b.

4.3. Correlation Between Radio and γ -ray Emission

We cross-matched our sample with the third *Fermi*-LAT AGN catalog (Ackermann et al. 2015) and found 73 sources (59% of our sample) detected in γ -rays. Combining with our previously observed ten sources in Paper II, we obtain a total of 79 sources, including 61 QSOs, 14 BL Lac objects, 3 radio galaxies (M87, NGC 6251, 3C 371), and 1 object (0648–165) with no optical identification. In our sample, BL Lac objects have a higher γ -ray detection rate (88%) than quasars (58%).

Figure 15 presents the flux density correlation between γ -rays and radio for all the 79

sources. We used the Pearson correlation test to reveal the flux density correlation between the radio and γ -rays. That gives a correlation with $\tau = 0.550$ and $P < 0.001$, where $\tau = 0$ means no correlation and $\tau = 1$ means strong correlation, and P gives the probability of no correlation. We should note that the three non-beamed AGNs (radio galaxies: M87, NGC 6251, and 3C 371) in our sample also follow the same γ -ray/radio flux density correlation, indicating that probably a universal γ -ray production mechanism, regardless of their difference in the central engine and jet power, is at work for diverse types of AGNs.

According to Ghirlanda et al. (2010), there is a strong correlation between the radio flux density at 20 GHz and the γ -ray flux above 100 MeV. Nieppola et al. (2011) even found a more significant correlation between both the flux densities and luminosities in γ -rays and 37-GHz single-dish radio data. Recently Fan et al. (2016) found a correlation between γ -ray and 1.4-GHz monochromatic radio luminosities. Ackermann et al. (2011) found that there is a correlation between γ -ray and 8.4-GHz (VLA and ATCA) / 15-GHz (OVRO single dish) radio luminosities. In the above studies, the authors used single-dish or low-resolution interferometer measurements of the radio flux densities. In contrast, our analysis is based on high-resolution high-frequency VLBI data; the correlation derived from our study is consistent with the previous works cited above but shows higher correlation coefficient. All these studies support the notion that the γ -ray emission zone is close to or same with the compact VLBI core.

In conclusion, our results give support to the strong correlation between the γ -ray and radio emission in AGNs, suggesting that the γ -ray emission zone is in the parsec-scale jet revealed by the 43 and 86 GHz VLBI images. The correlation is valid for diverse types of AGN over six orders of magnitude in radio luminosity and eight orders of magnitude in γ -rays, indicating that the general AGN population have a common γ -ray production mechanism, regardless of their different central engine and jet power.

5. Summary

We observed a sample of 124 bright and compact radio sources with the VLBA at 43 GHz between 2014 November and 2016 May. We achieved a highest angular resolution of ~ 0.2 mas and a typical image noise level of $0.5 \text{ mJy beam}^{-1}$. In our sample, 8 sources remain unresolved and are only detected with a compact core, 112 sources show one-sided jet structure, 3 sources have compact symmetric structures, and one source (0354+559) shows complex structure. We present the 43-GHz contour images of all the 124 sources and give comments on selected individual sources to highlight their properties in the context with other information from literature. The majority of these radio-loud AGNs have not been

previously imaged with VLBI at this frequency.

One of the main motivations of our project was to identify suitable target sources for the future mm-wavelength space VLBI program. From the distribution of source compactness on mas scales, $S_{\text{core}}/S_{\text{tot}}$, and sub-mas scales, $S_{\text{L}}/S_{\text{S}}$, 95 of the 124 sources have $S_{\text{L}} > 0.17$ Jy (about 10 times the baseline sensitivity of the SMVA), $S_{\text{core}}/S_{\text{tot}} > 0.5$ and $S_{\text{tot}} > 0.30$ Jy, and therefore there are 105 sources to be considered as targets for the SMVA.

For the 124 sources, we calculated the core brightness temperatures. Their median value is 7.92×10^{10} K, with a maximum of 2.54×10^{12} K at 43 GHz. This is somewhat higher than the inverse Compton catastrophe T_{b} limit and the equipartition limit, which can be explained by Doppler boosting of the relativistically beamed jet. We investigated the core brightness temperatures obtained from our project and other high-resolution VLBI observations from the literature at 2, 5, 8, 15, 22, 43, and 86 GHz. We find that the core brightness temperature is increasing below the break frequency ~ 7 GHz, and decreasing above 7 GHz. The break core brightness temperature value is 2×10^{12} K at ~ 7 GHz. The change of brightness temperature with (source rest frame) observing frequency is related to the resolution and synchrotron opacity changes with frequency.

We used 79 sources to test the correlation between radio and γ -ray flux densities and found tighter correlation compared to previous works. Our result supports the scenario that the location of the γ -ray emission is close to the 43 GHz VLBI core. Moreover our result also indicate that the radio– γ -ray correlation is universal and can be applicable to different types of AGNs.

Acknowledgments

This work was supported by the SKA pre-research funding granted by the National Key R&D Programme of China (2018YFA0404602, 2018YFA0404603), the Chinese Academy of Sciences (CAS, 114231KYSB20170003), and the Hungarian National Research, Development and Innovation Office (grant 2018-2.1.14-TÉT-CN-2018-00001). X.-P. Cheng was supported by Korea Research Fellowship Program through the National Research Foundation of Korea (NRF) funded by the Ministry of Science and ICT (2019H1D3A1A01102564). The VLBA observations were sponsored by Shanghai Astronomical Observatory through an MoU with the NRAO (Project code: BA111). This research has made use of data from the MOJAVE database that is maintained by the MOJAVE team (Lister et al. 2009). The MOJAVE program is supported under NASA-*Fermi* grants NNX15AU76G and NNX12A087G. The Very Long Baseline Array is a facility of the National Science Foundation operated under

cooperative agreement by Associated Universities, Inc. This research has made use of data from the OVRO 40-m monitoring program (Richards et al. 2011), which is supported in part by NASA grants NNX08AW31G, NNX11A043G and NNX14AQ89G and NSF grants AST-0808050 and AST-1109911. This work has made use of NASA Astrophysics Data System Abstract Service, and the NASA/IPAC Extragalactic Database (NED) which is operated by the Jet Propulsion Laboratory, California Institute of Technology, under contract with the National Aeronautics and Space Administration.

REFERENCES

- Acerro, F., Ackermann, M., Ajello, M., et al. 2015, *ApJ*, 218, 23 [2.1, 1]
- Ackermann, M., Ajello, M., Allafort, A., et al. 2011, *ApJ*, 741, 30 [4.3]
- Ackermann, M., Ajello, M., Atwood, W. B., et al. 2015, *ApJ*, 810, 14 [4.3]
- Agudo, I., Bach, U., Krichbaum, T. P., et al. 2007, *A&A*, 476, L17 [1]
- Agudo, I., Thum, C., Wiesemeyer, H., & Krichbaum, T. P. 2010, *ApJ*, 189, 1 [1]
- An, T., & Baan, W. A. 2012, *ApJ*, 760, 77 [3.1]
- An, T., Wu, X., & Frey, S. 2014, *Ap&SS*, 352, 825 (Paper I) [2.1]
- An, T., Cui, Y.-Z., Gabányi, K. É., et al. 2016, *AN*, 337, 65 [3.3]
- An, T., Wu, X.-P., & Hong, X. 2019, *Nat. Astron.*, 3, 1030 [2.2]
- An, T., Hong, X.Y., Zheng, W., et al. 2020, *Advances in Space Research*, 65, 850 [4.1]
- Antonucci, R. R. J., Hickson, P., Olszewski, E. W., & Miller, J. S. 1986, *AJ*, 92, 1 [3.3]
- Beasley, A. J., Gordon, D., Peck, A. B., et al. 2002, *ApJ*, 141, 13 [3.3]
- Begelman, M. C., Rees, M. J., & Sikora, M. 1994, *ApJ*, 429, L57 [4.2, 4.2]
- Blandford, R., Meier, D., & Readhead, A. 2019, *ARA&A*, 57, 467 [1]
- Bogers, W. J., Hes, R., Barthel, P. D., & Zensus, J. A. 1994, *A&AS*, 105, 91 [3.3]
- Bondi, M., Padrielli, L., Fanti, R., et al. 1996, *A&A*, 308, 415 [3.3]
- Charlot, P., Boboltz, D. A., Fey, A. L., et al. 2010, *AJ*, 139, 1713 [1]

- Cheng, X.-P., An, T., Hong, X.-Y., et al. 2018, *ApJ*, 234, 17 (Paper II) [1, 2.1, 4.1, 4.2, 2, 14]
- Condon, J. J., Cotton, W. D., Greisen, E. W., et al. 1998, *AJ*, 115, 1693 [3.3]
- Cooper, N. J., Lister, M. L., & Kochanzyk, M. D. 2007, *ApJ*, 171, 376 [3.3]
- Dallacasa, D., Stanghellini, C., Centonza, M., & Fanti, R. 2000, *A&A*, 363, 887 [3.3]
- de Bruyn, A. G. 1989, *A&A*, 226, L13 [3.3]
- de Vries, W. H., O’Dea, C. P., Barthel, P. D., & Thompson, D. J. 2000, *A&AS*, 143, 181 [3.3]
- Deller, A. T., Tingay, S. J., Bailes, M. & West, C. 2007, *PASP*, 119, 318 [2.2]
- Deller, A. T., Brisken, W. F., Phillips, C. J. et al. 2011, *PASP*, 123, 275 [2.2]
- Dermer, C. D., & Schlickeiser, R. 1993, *ApJ*, 416, 458 [1]
- Dodson, R., Fomalont, E. B., Wiik, K., et al. 2008, *ApJ*, 175, 314 [1, 3.3]
- Fan, J. H., Yang, J. H., Liu, Y., et al. 2016, *ApJ*, 226, 20 [4.3]
- Fermi-LAT collaboration 2019, e-print, arXiv:1905.10771 [1]
- Fey, A. L., & Charlot, P. 2000, *ApJ*, 128, 17 [3.3]
- Fey, A. L., Ma, C., Arias, E. F., et al. 2004, *AJ*, 127, 3587 [3.3]
- Fey, A. L., Gordon, D., Jacobs, C. S., et al. 2015, *AJ*, 150, 58 [3.3]
- Fomalont, E. B., Frey, S., Paragi, Z., et al. 2000, *ApJ*, 131, 95 [3.3]
- Fomalont, E. B., Petrov, L., MacMillan, D. S., Gordon, D., & Ma, C. 2003, *AJ*, 126, 2562 [3.3]
- Frey, S., Gurvits, L. I., Altschuler, D. R., et al. 2000, *PASJ*, 52, 975 [1]
- Gallimore, J. F., Baum, S. A., & O’Dea, C. P. 2004, *ApJ*, 613, 794 [1]
- Ghirlanda, G., Ghisellini, G., Tavecchio, F., & Foschini, L. 2010, *MNRAS*, 407, 791 [4.3]
- Greisen, E. W. 2003, *Information Handling in Astronomy - Historical Vistas, Astrophysics and Space Science Library*, Vol. 285 (Springer), p. 109 [2.3]

- Hada, K., Kino, M., Doi, A., et al. 2016, ApJ, 817, 131 [3.3]
- Halzen, F., Kheirandish, A., Weisgarber, T., & Wakely, S. P. 2019, ApJ, 874, L9 [1]
- Helmboldt, J. F., Taylor, G. B., Tremblay, S., et al. 2007, ApJ, 658, 203 [3.3]
- Hirabayashi, H., Hirose, H., Kobayashi, H. et al. 1998, Sci., 281, 1825 [1]
- Hong, X., Shen, Z., An, T. & Liu, Q. 2014, Acta Astronaut., 102, 217 [4.1]
- Horiuchi, S., Fomalont, E. B., Taylor, W. K., et al. 2004, ApJ, 616, 110 [4.2, 14]
- Hutchings, J. B., Dewey, A., Chaytor, D., et al. 1998, PASP, 110, 111 [3.3]
- IceCube Collaboration, Aartsen, M. G., Ackermann, M., et al. 2018, Sci., 361, eaat1378 [1]
- IceCube Collaboration, Aartsen, M. G., Ackermann, M., et al. 2018, Sci., 361, 147 [1]
- Jorstad, S. G., Marscher, A. P., Morozova, D. A., et al. 2017, ApJ, 846, 98 [1, 2.3]
- Kardashev, N. S. 2000, Astron. Rep., 44, 719 [4.2]
- Kardashev, N. S. 2017, Astron. Rep., 61, 310 [4.1]
- Kardashev, N. S., Khartov, V. V., Abramov, V. V. et al. 2013, Astron. Rep., 57, 153 [1]
- Kellermann, K. I., & Pauliny-Toth, I. I. K. 1969, ApJ, 155, L71 [1, 4.2, 4.2]
- Kellermann, K. I., Vermeulen, R. C., Zensus, J. A., & Cohen, M. H. 1998, AJ, 115, 1295 [3.3]
- Kellermann, K. I. 2002, PASA, 19, 77 [4.2]
- Kharb, P., Lister, M. L., & Cooper, N. J. 2010, ApJ, 710, 764 [3.3]
- Kovalev, Y. Y., Kellermann, K. I., Lister, M. L. et al. 2005, AJ, 130, 2473 [1, 4.1, 4.2, 14]
- Kovalev, Y. Y., Lobanov, A. P., Pushkarev, A. B., & Zensus, J. A. 2008, A&A, 483, 759 [4.2]
- Kovalev, Y. Y., Kardashev, N. S., Kellermann, K. I., et al. 2016, ApJ, 820, L9 [1]
- Krichbaum, T. P. & Witzel, A. 1992, in: Variability of Blazars, ed. E. Valtaoja and M. Valtonen (Cambridge University Press), p. 205 [2.1]
- Kutkin, A. M., Paschenko, I. N., Lisakov, N. N., et al. 2018, MNRAS, 475, 4994 [1]

- Laing, R. A., Riley, J. M., & Longair, M. S. 1983, MNRAS, 204, 151 [3.3]
- Lanyi, G. E., Boboltz, D. A., Charlot, P. et al. 2010, AJ, 139, 1695 [2.1]
- Lee, S.-S., Lobanov, A. P., Krichbaum, T. P., et al. 2008, AJ, 136, 159 [1, 4.1, 4.2, 14]
- Lee, S.-S., Lobanov, A. P., Krichbaum, T. P., & Zensus, J. A. 2016, ApJ, 826, 135 [1]
- Lister, M. L. 2001, ApJ, 562, 208 [1, 2.1]
- Lister, M. L., Cohen, M. H., Homan, D. C., et al. 2009, AJ, 138, 1874 [3.3, 5]
- Lister, M. L., Aller, M. F., Aller, H. D., et al. 2013, AJ, 146, 120 [3.3]
- Lobanov, A. P. 2005, e-print, arXiv:astro-ph/0503225 [2.4]
- Lister, M. L., Aller, M. F., Aller, H. D., et al. 2016, AJ, 152, 12 [1, 3.3]
- Lister, M. L., Homan, D. C., Hovatta, T., et al. 2019, ApJ, 874, 43 [3.3]
- Marcha, M. J. M., Browne, I. W. A., Impey, C. D., & Smith, P. S. 1996, MNRAS, 281, 425 [3.3]
- Marscher, A. P. 1995, Proc. Nat. Acad. Sci., 92, 11439 [1]
- Marscher, A. P., Jorstad, S. G., Mattox, J. R. & Wehrle, A. E. 2002, ApJ, 577, 85 [2.1]
- Moellenbrock, G. A., Fujisawa, K., Preston, R. A., et al. 1996, AJ, 111, 2174 [1, 4.2, 14]
- Murphy, D. W., Browne, I. W. A. & Perley, R. A. 1993, MNRAS, 264, 298 [3.3]
- Nair, D. G., Lobanov, A. P., Krichbaum, T. P., et al. 2019, A&A, 622, A92 [1, 2.3, 4.2, 14]
- Nieppola, E., Tornikoski, M., Valtaoja, E., et al. 2011, A&A, 535, A69 [4.3]
- Orienti, M., Dallacasa, D., Tinti, S., & Stanghellini, C. 2006, A&A, 450, 959 [3.3]
- O’Sullivan, S. P., & Gabuzda, D. C. 2009, MNRAS, 400, 26 [4.2]
- Owen, F. N., Eilek, J. A., & Kassim, N. E. 2000, ApJ, 543, 611 [3.3]
- Pilipenko, S. V., Kovalev, Y. Y., Andrianov, A. S., et al. 2018, MNRAS, 474, 3523 [1]
- Perley, R. A., Bridle, A. H., & Willis, A. G. 1984, ApJ, 54, 291 [3.3]
- Petrov, L., Kovalev, Y. Y., Fomalont, E., & Gordon, D. 2005, AJ, 129, 1163 [3.3]

- Piner, B. G., Pant, N., & Edwards, P. G. 2010, *ApJ*, 723, 1150 [1]
- Piner, B. G., Pushkarev, A. B., Kovalev, Y. Y., et al. 2012, *ApJ*, 758, 84 [3.3]
- Polatidis, A. G., Wilkinson, P. N., Xu, W., et al. 1995, *ApJ*, 98, 1 [3.3]
- Polatidis, A. G., & Conway, J. E. 2003, *PASA*, 20, 69 [3.1]
- Punsly, B. 1995, *AJ*, 109, 1555 [3.3]
- Pushkarev, A. B., & Kovalev, Y. Y. 2012, *A&A*, 544, A34 [3.3, 4.2, 14]
- Readhead, A. C. S. 1994, *ApJ*, 426, 51 [1, 4.2, 4.2]
- Rector, T. A., & Stocke, J. T. 2001, *AJ*, 122, 565 [3.3]
- Reid, A., Shone, D. L., Akujor, C. E., et al. 1995, *A&AS*, 110, 213 [3.3]
- Reines, F. 1960, *Ann. Rev. Nucl. Part. Sci.*, 10, 1 [1]
- Richards, J. L., Max-Moerbeck, W., Pavlidou, V. et al. 2011, *ApJ*, 194, 29 [3.3, 5]
- Ros, E., Kadler, M., Perucho, M., et al. 2020, *A&A*, 633, L1 [1]
- Sambruna, R. M., Gambill, J. K., Maraschi, L., et al. 2004, *ApJ*, 608, 698 [3.3]
- Scott, W. K., Fomalont, E. B., Horiuchi, S., et al. 2004, *ApJ*, 155, 33 [3.3]
- Shepherd, M. C. 1997, *Astronomical Data Analysis Software and Systems VI*, ASP Conf. Ser. 125, 77 [2.3]
- Sikora, M., Begelman, M. C., & Rees, M. J. 1994, *ApJ*, 421, 153 [1]
- Sokolovsky, K. V., Kovalev, Y. Y., Pushkarev, A. B., & Lobanov, A. P. 2011, *A&A*, 532, A38 [4.2]
- Stanghellini, C., O’Dea, C. P., Baum, S. A., et al. 1997, *A&A*, 325, 943 [3.3]
- Stanghellini, C., O’Dea, C. P., Dallacasa, D., et al. 1998, *A&AS*, 131, 303 [3.1, 3.3]
- Stanghellini, C., Dallacasa, D., O’Dea, C. P., et al. 2001, *A&A*, 377, 377 [3.3]
- Taylor, G. B., Vermeulen, R. C., Readhead, A. C. S., et al. 1996, *ApJ*, 107, 37 [3.3]
- Tingay, S. J., Preston, R. A., Lister, M. L., et al. 2001, *ApJ*, 549, L55 [1]
- Tingay, S. J., Jauncey, D. L., King, E. A., et al. 2003, *PASJ*, 55, 351 [3.3]

Torniainen, I., Tornikoski, M., Teräsraanta, H., Aller, M. F., & Aller, H. D. 2005, *A&A*, 435, 839 [3.3]

Tschager, W., Schilizzi, R. T., Röttgering, H. J. A., Snellen, I. A. G., & Miley, G. K. 2000, *A&A*, 360, 887 [3.3]

Ulvestad, J., Johnston, K., Perley, R., & Fomalont, E. 1981, *AJ*, 86, 1010 [3.3]

Véron-Cetty, M.-P., & Véron, P. 2006, *A&A*, 455, 773 [3.3]

Zhao, W., Hong, X., An, T., et al. 2019, *Galaxies*, 7, 86 [3.3]

Table 1. General Source Properties

IAU Name (1)	Alias (2)	Sess. (3)	R.A. (J2000) (4)	Dec. (J2000) (5)	z (6)	Opt. Class (7)	Comm. (8)	S_{Fermi} ($10^{-10} \text{ph cm}^{-2} \text{s}^{-1}$) (9)
0048–071	OB –082	C	00 51 08.20982	–06 50 02.2291	1.975	QSO	Y	12
0106+013	4C +01.02	B	01 08 38.77110	+01 35 00.3713	2.099	QSO	Y	64
0113–118		C	01 16 12.52203	–11 36 15.4348	0.671	QSO	Y	15
0119+041	OC +033	C	01 21 56.86170	+04 22 24.7342	0.637	QSO	Y	...
0122–003	UM 321	C	01 25 28.84383	–00 05 55.9322	1.077	QSO	Y	...
0130–171	OC –150	B	01 32 43.48746	–16 54 48.5218	1.020	QSO	Y	21
0149+218		C	01 52 18.05904	+22 07 07.6997	1.320	QSO	Y	...
0202–172		C	02 04 57.67434	–17 01 19.8405	1.739	QSO	Y	7
0208+106		C	02 11 13.77363	+10 51 34.7986	0.200	BL Lac	Y	26
0221+067	4C +06.11	B	02 24 28.42819	+06 59 23.3415	0.511	QSO	Y	...
0224+671	4C +67.05	C	02 28 50.05149	+67 21 03.0293	0.523	QSO	Y	...
0229+131	4C +13.14	C	02 31 45.89406	+13 22 54.7162	2.059	QSO	Y	...
0239+108	OD +166	C	02 42 29.17085	+11 01 00.7280	2.680	QSO	Y	...
0241+622		C	02 44 57.69671	+62 28 06.5157	0.045	QSO	Y	...
0306+102	OE +110	C	03 09 03.62350	+10 29 16.3410	0.862	QSO	Y	15
0309+411	NRAO 128	B	03 13 01.96212	+41 20 01.1835	0.136	G	Y	...
0322+222		C	03 25 36.81436	+22 24 00.3655	2.066	QSO	N	11
0354+559		B	03 58 30.18819	+56 06 44.4602	...	U	Y	...
0400+258	CTD 026	C	04 03 05.58608	+26 00 01.5027	2.109	QSO	Y	...
0403–132		C	04 05 34.00339	–13 08 13.6908	0.571	QSO	Y	...
0405–123		B	04 07 48.43097	–12 11 36.6593	0.573	QSO	N	...
0420+417	4C +41.11	C	04 23 56.00979	+41 50 02.7129	...	BL Lac	N	29
0451–282	OF –285	B	04 53 14.64679	–28 07 37.3265	2.559	QSO	N	19
0507+179		C	05 10 02.36913	+18 00 41.5816	0.416	QSO	Y	12
0529+075	OG 050	C	05 32 38.99846	+07 32 43.3449	1.254	QSO	Y	41
0605–085	OC –010	B	06 07 59.69923	–08 34 49.9781	0.870	QSO	Y	18
0627–199		B	06 29 23.76185	–19 59 19.7235	1.724	BL Lac	N	25
0633+734		C	06 39 21.96122	+73 24 58.0403	1.850	QSO	N	6
0648–165		C	06 50 24.58186	–16 37 39.7255	...	U	Y	14
0657+172		B	07 00 01.52553	+17 09 21.7014	...	U	Y	...
0708+506		B	07 12 43.68355	+50 33 22.7069	0.502	BL Lac	N	17
0723–008		B	07 25 50.63996	–00 54 56.5441	0.128	BL Lac	Y	11
0730+504		C	07 33 52.52059	+50 22 09.0621	0.720	QSO	N	7
0736+017	OI 061	C	07 39 18.03390	+01 37 04.6177	0.189	QSO	Y	25
0738+313	OI 363	C	07 41 10.70331	+31 12 00.2292	0.631	QSO	Y	...

Table 1—Continued

IAU Name (1)	Alias (2)	Sess. (3)	R.A. (J2000) (4)	Dec. (J2000) (5)	z (6)	Opt. Class (7)	Comm. (8)	S_{Fermi} ($10^{-10}\text{ph cm}^{-2}\text{s}^{-1}$) (9)
0742+103		C	07 45 33.05952	+10 11 12.6922	2.624	QSO	Y	...
0743–006	OI –072	C	07 45 54.08232	–00 44 17.5399	0.996	QSO	Y	...
0754+100	OI +090.4	C	07 57 06.64295	+09 56 34.8522	0.266	BL Lac	N	20
0805+410		C	08 08 56.65204	+40 52 44.8888	1.418	QSO	N	...
0805–077		B	08 08 15.53603	–07 51 09.8862	1.837	QSO	N	150
0808+019	OJ 014	C	08 11 26.70732	+01 46 52.2201	1.148	BL Lac	N	13
0821+394	4C +39.23	C	08 24 55.48386	+39 16 41.9040	1.216	QSO	N	4
0838+133	3C 207	C	08 40 47.58843	+13 12 23.5637	0.681	QSO	Y	8
0847–120		C	08 50 09.63563	–12 13 35.3762	0.566	QSO	N	31
0859–140	OJ –199	C	09 02 16.83092	–14 15 30.8753	1.333	QSO	Y	...
0906+015	4C +01.24	C	09 09 10.09160	+01 21 35.6177	1.024	QSO	Y	32
0917+624	OK 630	C	09 21 36.23107	+62 15 52.1803	1.447	QSO	N	8
0925–203		B	09 27 51.82431	–20 34 51.2324	0.348	QSO	N	6
0945+408	4C +40.24	B	09 48 55.33815	+40 39 44.5869	1.249	QSO	Y	4
1032–199		B	10 35 02.15530	–20 11 34.3595	2.198	QSO	N	...
1036+054		C	10 38 46.77988	+05 12 29.0865	0.473	QSO	Y	...
1038+064	4C +06.41	C	10 41 17.16250	+06 10 16.9235	1.265	QSO	N	11
1045–188		C	10 48 06.62060	–19 09 35.7268	0.595	QSO	Y	...
1049+215	4C +21.28	C	10 51 48.78907	+21 19 52.3137	1.300	QSO	N	...
1124–186	OM –148	C	11 27 04.39245	–18 57 17.4418	1.048	QSO	Y	34
1149–084		B	11 52 17.20951	–08 41 03.3138	2.367	QSO	N	12
1150+497	4C +49.22	B	11 53 24.46663	+49 31 08.8301	0.334	QSO	Y	8
1213–172		C	12 15 46.75176	–17 31 45.4032	...	U	N	...
1219+044	4C +04.42	B	12 22 22.54962	+04 13 15.7761	0.966	QSO	Y	13
1228+126	3C 274	B	12 30 49.42338	+12 23 28.0438	0.004	G	Y	14
1243–072		C	12 46 04.23210	–07 30 46.5748	1.286	QSO	N	...
1257+519		B	12 59 31.17401	+51 40 56.2607	0.405	G	N	...
1306+360		B	13 08 23.70914	+35 46 37.1639	1.055	QSO	N	11
1324+224		C	13 27 00.86131	+22 10 50.1628	1.398	QSO	Y	19
1329–049	OP –050	B	13 32 04.46467	–05 09 43.3056	2.150	QSO	N	50
1354+195	4C +19.44	C	13 57 04.43666	+19 19 07.3723	0.720	QSO	N	...
1417+385		C	14 19 46.61376	+38 21 48.4750	1.831	QSO	N	5
1435+638	VIPS 0792	C	14 36 45.80216	+63 36 37.8663	2.068	QSO	Y	...
1502+106	OR 103	C	15 04 24.97978	+10 29 39.1984	1.838	QSO	N	401
1504–166		C	15 07 04.78696	–16 52 30.2671	0.876	QSO	Y	...

Table 1—Continued

IAU Name (1)	Alias (2)	Sess. (3)	R.A. (J2000) (4)	Dec. (J2000) (5)	z (6)	Opt. Class (7)	Comm. (8)	S_{Fermi} ($10^{-10} \text{ph cm}^{-2} \text{s}^{-1}$) (9)
1514+004		C	15 16 40.21905	+00 15 01.9087	0.052	G	Y	...
1514+197		C	15 16 56.79616	+19 32 12.9919	1.070	BL Lac	N	5
1532+016		C	15 34 52.45368	+01 31 04.2064	1.425	QSO	N	...
1546+027		C	15 49 29.43685	+02 37 01.1631	0.414	QSO	N	18
1548+056	4C +05.64	B	15 50 35.26924	+05 27 10.4484	1.417	QSO	Y	10
1606+106	4C +10.45	C	16 08 46.20319	+10 29 07.7756	1.232	QSO	N	16
1636+473	4C +47.44	C	16 37 45.13056	+47 17 33.8310	0.735	QSO	N	18
1637+826	NGC 6251	C	16 32 31.96989	+82 32 16.3999	0.024	G	Y	11
1639–062		C	16 42 02.17772	–06 21 23.6952	1.514	BL Lac	N	11
1642+690	4C +69.21	B	16 42 07.84850	+68 56 39.7564	0.751	QSO	N	...
1655+077		C	16 58 09.01147	+07 41 27.5403	0.621	QSO	N	...
1656+477		C	16 58 02.77959	+47 37 49.2307	1.615	QSO	N	...
1657–261		B	17 00 53.15406	–26 10 51.7253	...	U	N	...
1659+399		B	17 01 24.63481	+39 54 37.0915	0.507	BL Lac	N	...
1716+686		B	17 16 13.93800	+68 36 38.7446	0.777	QSO	Y	12
1725+044		C	17 28 24.95272	+04 27 04.9137	0.293	QSO	N	13
1726+455		C	17 27 27.65080	+45 30 39.7312	0.717	QSO	N	15
1800+440		C	18 01 32.31482	+44 04 21.9002	0.663	QSO	N	4
1806+456		B	18 08 21.88588	+45 42 20.8663	0.830	QSO	N	...
1807+698	3C 371	B	18 06 50.68064	+69 49 28.1085	0.051	BL Lac	N	38
1842+681		C	18 42 33.64169	+68 09 25.2277	0.472	QSO	N	...
1849+670		C	18 49 16.07228	+67 05 41.6802	0.657	QSO	N	74
1920–211	OV –235	B	19 23 32.18981	–21 04 33.3330	0.874	QSO	N	83
1926+611		B	19 27 30.44262	+61 17 32.8792	...	BL Lac	Y	9
1957–135		C	20 00 42.14510	–13 25 33.5338	0.222	QSO	N	...
1958–179		C	20 00 57.09045	–17 48 57.6727	0.652	QSO	N	25
2007+777		B	20 05 30.99853	+77 52 43.2475	0.342	BL Lac	Y	11
2021+317	4C +31.56	C	20 23 19.01734	+31 53 02.3060	0.356	BL Lac	Y	...
2021+614	OW +637	B	20 22 06.68174	+61 36 58.8047	0.227	G	Y	...
2022–077	NRAO 0629	C	20 25 40.66041	–07 35 52.6892	1.388	QSO	N	101
2023+335		C	20 25 10.84211	+33 43 00.2144	0.219	QSO	N	41
2029+121	OW +149	B	20 31 54.99427	+12 19 41.3403	1.215	QSO	Y	12
2126–158	OX –146	C	21 29 12.17590	–15 38 41.0416	3.268	QSO	Y	...
2134+004		B	21 36 38.58630	+00 41 54.2129	1.941	QSO	Y	...
2135+508		C	21 37 00.98621	+51 01 36.1290	...	U	N	...

Table 1—Continued

IAU Name (1)	Alias (2)	Sess. (3)	R.A. (J2000) (4)	Dec. (J2000) (5)	z (6)	Opt. Class (7)	Comm. (8)	S_{Fermi} ($10^{-10} \text{ph cm}^{-2} \text{s}^{-1}$) (9)
2141+175	OX 169	B	21 43 35.54457	+17 43 48.7874	0.213	QSO	Y	45
2142+110		B	21 45 18.77507	+11 15 27.3123	0.548	QSO	N	...
2144+092		C	21 47 10.16297	+09 29 46.6723	1.113	QSO	N	35
2155–152		B	21 58 06.28190	–15 01 09.3278	0.672	QSO	Y	11
2201+171		C	22 03 26.89368	+17 25 48.2476	1.076	QSO	N	65
2209+236		C	22 12 05.96631	+23 55 40.5437	1.125	QSO	Y	10
2216–038	4C –03.79	C	22 18 52.03773	–03 35 36.8796	0.901	QSO	N	...
2223+210	DA 580	B	22 25 38.04713	+21 18 06.4150	1.959	QSO	Y	...
2227–088	PHL 5225	C	22 29 40.08434	–08 32 54.4356	1.560	QSO	Y	43
2234+282	CTD 135	C	22 36 22.47085	+28 28 57.4132	0.790	BL Lac	Y	51
2243–123		C	22 46 18.23198	–12 06 51.2775	0.632	QSO	Y	...
2308+341		C	23 11 05.32880	+34 25 10.9056	1.817	QSO	N	43
2318+049		C	23 20 44.85660	+05 13 49.9524	0.623	QSO	Y	...
2320–035		C	23 23 31.95375	–03 17 05.0239	1.411	QSO	N	21
2325+093	OZ 042	C	23 27 33.58058	+09 40 09.4626	1.841	QSO	N	20
2342–161		C	23 45 12.46232	–15 55 07.8345	0.621	QSO	N	42
2344+092		C	23 46 36.83855	+09 30 45.5147	0.677	QSO	N	...
2345–167	OZ –176	C	23 48 02.60853	–16 31 12.0222	0.576	QSO	N	16
2351–154	OZ –187	C	23 54 30.19518	–15 13 11.2129	2.675	QSO	N	...

Note. — (1) Source name (B1950.0); (2) Other commonly used source name; (3) Observation session; (4) Right ascension (J2000); (5) Declination (J2000); (6) Redshift; (7) Optical classification, where QSO = quasar, BL Lac = BL Lac object, G = active galaxy, and U = unidentified; (8) Source comments available in Sect. 3.3; (9) γ -ray flux from [Acero et al. \(2015\)](#).

Table 2. Log of VLBA Observations

Session	Observation Code	Observation Date yyyy/mm/dd	ν GHz	τ_{int} min	No. of sources	Reference
(1)	(2)	(3)	(4)	(5)	(6)	(7)
A	BA111A – BA111F	2014/11/21 – 2016/05/06	43/86	80	10	Cheng et al. (2018)
B	BA111G – BA111I	2015/06/19 – 2016/04/22	43	28	40	This paper
C	BA111J – BA111M	2015/10/10 – 2016/02/09	43	14	84	This paper

Note. — (1) Observing session; (2) VLBA observation code; (3) Range of observation dates; (4) Observing frequency; (5) Integration time for each individual source; (6) Number of sources observed and imaged; (7) References.

Table 3. Image Parameters

IAU Name (1)	Observation yyyy-mm-dd (2)	B_{maj} (mas) (3)	B_{min} (mas) (4)	$B_{\text{P.A.}}$ ($^{\circ}$) (5)	S_{tot} (Jy) (6)	S_{peak} (Jy beam $^{-1}$) (7)	σ (mJy beam $^{-1}$) (8)	S_{S} (Jy) (9)	B_{S} (M λ) (10)	S_{L} (Jy) (11)	B_{L} (M λ) (12)
0048–071	2015-11-30	0.67	0.21	16.7	0.480	0.412	0.22	0.48	27	0.41	270
0106+013	2015-06-19	0.44	0.18	–4.4	1.202	0.801	0.70	1.09	24	0.75	406
0113–118	2015-11-30	0.67	0.21	12.7	0.698	0.568	0.85	0.70	27	0.55	260
0119+041	2015-11-30	0.52	0.21	14.2	0.546	0.345	0.40	0.54	30	0.33	296
0122–003	2015-11-30	0.63	0.19	18.4	0.425	0.256	0.17	0.40	27	0.30	286
0130–171	2015-06-19	0.44	0.16	–5.1	0.597	0.390	0.58	0.59	20	0.23	438
0149+218	2015-11-30	0.49	0.20	16.8	1.160	0.970	1.46	1.14	33	0.81	336
0202–172	2015-11-30	0.72	0.20	12.6	1.015	0.676	1.20	0.82	31	0.65	244
0208+106	2015-11-30	0.51	0.22	13.4	0.530	0.314	0.30	0.49	33	0.25	306
0221+067	2015-06-19	0.42	0.17	–2.5	1.020	0.693	0.40	1.01	29	0.34	438
0224+671	2015-11-30	0.44	0.24	–22.1	0.519	0.294	0.89	0.49	33	0.21	360
0229+131	2015-11-30	0.54	0.25	15	0.692	0.442	0.48	0.66	27	0.48	306
0239+108	2015-11-30	0.71	0.29	24.3	0.240	0.189	0.17	0.24	26	0.14	293
0241+622	2015-11-30	0.45	0.26	–30	0.825	0.693	0.70	0.83	32	0.44	385
0306+102	2015-11-30	0.59	0.26	17.3	0.899	0.776	0.35	0.90	26	0.67	291
0309+411	2015-06-19	0.44	0.16	10.3	0.735	0.388	0.33	0.74	31	0.17	510
0322+222	2015-11-30	0.49	0.26	7.7	0.553	0.487	0.34	0.55	30	0.46	325
0354+559	2015-06-19	0.44	0.17	19.7	0.521	0.211	0.40	0.42	28	0.21	495
0400+258	2015-11-30	0.47	0.21	10.7	0.237	0.112	0.23	0.23	31	0.11	331
0403–132	2015-11-30	0.84	0.26	15.9	0.337	0.280	0.70	0.34	20	0.24	227
0405–123	2015-06-19	0.43	0.14	–7.3	0.801	0.389	0.95	0.80	23	0.14	356
0420+417	2015-11-30	0.45	0.25	–5.3	0.300	0.222	0.64	0.28	33	0.23	376
0451–282	2015-06-19	0.46	0.17	–4.4	0.958	0.740	0.89	0.96	23	0.64	400
0507+179	2015-11-30	0.52	0.26	10.9	2.487	2.440	1.20	2.48	29	2.46	308
0529+075	2015-11-30	0.58	0.27	13.7	1.316	1.040	0.80	1.31	27	0.85	277
0605–085	2015-06-19	0.47	0.17	–9.9	2.047	0.784	1.70	2.04	24	0.49	407
0627–199	2015-06-19	0.44	0.17	–3.6	0.423	0.340	0.80	0.43	22	0.29	440
0633+734	2015-11-30	0.53	0.23	–16.7	0.411	0.380	0.45	0.41	30	0.34	310
0648–165	2015-11-30	0.94	0.23	20.9	0.501	0.350	0.53	0.50	23	0.33	217
0657+172	2015-06-19	0.43	0.17	–4.5	0.335	0.184	0.48	0.33	32	0.13	460
0708+506	2015-06-19	0.42	0.17	7.3	0.370	0.330	0.27	0.37	30	0.28	540
0723–008	2015-06-19	0.48	0.16	–11.8	1.771	0.573	1.60	1.78	29	0.45	400
0730+504	2015-10-10	0.39	0.17	15.8	0.215	0.127	0.50	0.21	29	0.10	460
0736+017	2015-10-10	0.46	0.17	–11.5	0.706	0.424	1.06	0.71	30	0.18	415
0738+313	2015-10-10	0.45	0.19	2.7	1.142	0.467	1.00	0.99	32	0.23	473

Table 3—Continued

IAU Name (1)	Observation yyyy-mm-dd (2)	B_{maj} (mas) (3)	B_{min} (mas) (4)	$B_{\text{P.A.}}$ ($^{\circ}$) (5)	S_{tot} (Jy) (6)	S_{peak} (Jy beam $^{-1}$) (7)	σ (mJy beam $^{-1}$) (8)	S_{S} (Jy) (9)	B_{S} (M λ) (10)	S_{L} (Jy) (11)	B_{L} (M λ) (12)
0742+103	2015-10-10	0.62	0.21	−14.1	0.412	0.257	0.50	0.35	32	0.23	368
0743−006	2015-10-10	0.40	0.17	−1.4	0.491	0.177	0.48	0.42	30	0.14	403
0754+100	2015-10-10	0.43	0.17	−5.8	0.669	0.480	0.38	0.63	32	0.31	420
0805+410	2015-10-10	0.45	0.18	2.3	0.844	0.643	0.98	0.85	31	0.37	490
0805−077	2015-06-19	0.43	0.18	1.1	0.601	0.534	0.70	0.61	29	0.46	404
0808+019	2015-10-10	0.46	0.18	−6.7	1.175	1.100	0.66	1.17	30	1.05	414
0821+394	2015-10-10	0.42	0.18	0.3	0.320	0.106	0.37	0.32	31	0.12	500
0838+133	2015-10-10	0.40	0.17	−0.4	0.711	0.436	0.65	0.69	33	0.27	428
0847−120	2015-10-10	0.45	0.18	−2.4	0.837	0.743	0.75	0.84	28	0.68	422
0859−140	2015-10-10	0.49	0.18	−9.2	0.198	0.086	0.55	0.20	27	0.10	430
0906+015	2015-10-10	0.46	0.18	−7.8	0.789	0.402	0.70	0.75	23	0.32	402
0917+624	2015-10-10	0.43	0.17	−18.4	0.572	0.420	0.50	0.57	32	0.39	406
0925−203	2015-06-19	0.43	0.16	−4.7	0.370	0.249	0.70	0.38	23	0.27	424
0945+408	2015-06-19	0.43	0.16	1.8	0.308	0.152	0.58	0.30	33	0.05	455
1032−199	2015-06-19	0.43	0.17	−1.7	0.335	0.234	0.42	0.31	27	0.24	432
1036+054	2015-10-10	0.52	0.17	−10.8	0.332	0.198	0.90	0.32	28	0.22	415
1038+064	2015-10-10	0.63	0.18	−15.7	0.381	0.326	0.39	0.37	27	0.23	414
1045−188	2015-10-10	0.49	0.16	−9.6	0.738	0.423	0.90	0.74	20	0.19	420
1049+215	2015-10-10	0.43	0.16	−1.3	0.246	0.128	0.30	0.25	30	0.05	460
1124−186	2015-10-10	0.49	0.17	−7.7	1.269	1.100	1.20	1.28	22	0.93	440
1149−084	2015-06-19	0.42	0.17	−5.6	0.326	0.126	0.48	0.32	28	0.06	410
1150+497	2015-06-19	0.45	0.17	7.8	0.837	0.617	0.44	0.81	31	0.52	480
1213−172	2015-10-10	0.44	0.14	−3.7	0.560	0.158	0.58	0.54	25	0.19	370
1219+044	2015-06-20	0.44	0.17	−5.1	0.628	0.563	0.30	0.63	25	0.37	418
1228+126	2015-06-20	0.42	0.18	−3.5	1.331	0.604	0.68	1.26	28	0.29	442
1243−072	2016-02-09	0.73	0.20	21.6	0.928	0.754	0.40	0.91	62	0.65	207
1257+519	2015-06-20	0.42	0.18	−2.1	0.339	0.289	0.18	0.34	31	0.26	530
1306+360	2015-06-20	0.41	0.18	−3.5	0.669	0.625	0.28	0.67	33	0.54	520
1324+224	2016-02-09	0.53	0.20	25.4	0.314	0.281	0.24	0.31	84	0.29	248
1329−049	2015-06-20	0.47	0.17	−6.5	0.811	0.557	0.52	0.68	25	0.40	422
1354+195	2016-02-09	0.53	0.20	26.1	1.254	0.583	0.28	1.06	82	0.43	244
1417+385	2016-02-09	0.49	0.31	32.1	0.172	0.145	0.14	0.17	82	0.15	268
1435+638	2016-02-09	0.56	0.28	40.7	0.267	0.099	0.45	0.25	28	0.16	368
1502+106	2016-02-09	0.54	0.25	26.7	2.909	2.770	0.48	2.90	32	2.85	234
1504−166	2016-02-09	0.75	0.22	15	0.553	0.511	0.24	0.55	44	0.52	204

Table 3—Continued

IAU Name (1)	Observation yyyy-mm-dd (2)	B_{maj} (mas) (3)	B_{min} (mas) (4)	$B_{\text{P.A.}}$ ($^{\circ}$) (5)	S_{tot} (Jy) (6)	S_{peak} (Jy beam $^{-1}$) (7)	σ (mJy beam $^{-1}$) (8)	S_{S} (Jy) (9)	B_{S} (M λ) (10)	S_{L} (Jy) (11)	B_{L} (M λ) (12)
1514+004	2016-02-09	0.60	0.22	21.7	0.529	0.299	0.35	0.39	68	0.38	210
1514+197	2016-02-09	0.53	0.21	28.1	0.628	0.501	0.12	0.63	32	0.59	253
1532+016	2016-02-09	0.56	0.19	19.5	0.419	0.223	0.35	0.44	30	0.24	291
1546+027	2016-02-09	0.55	0.22	12.6	2.516	2.060	0.98	2.51	31	1.71	266
1548+056	2015-06-20	0.43	0.18	−1.8	1.056	0.448	0.59	0.84	31	0.23	414
1606+106	2016-02-09	0.50	0.21	16.6	0.549	0.496	0.23	0.57	58	0.48	287
1636+473	2016-02-09	0.46	0.21	16.4	0.462	0.374	0.48	0.45	85	0.30	333
1637+826	2016-02-09	0.56	0.22	4.4	0.432	0.258	0.21	0.43	25	0.11	267
1639−062	2016-02-09	0.66	0.21	21.1	0.709	0.628	0.24	0.70	69	0.59	268
1642+690	2015-06-20	0.57	0.21	7.4	0.780	0.489	1.40	0.76	27	0.42	312
1655+077	2016-02-09	0.55	0.23	15.5	0.480	0.348	0.73	0.44	78	0.30	295
1656+477	2016-02-09	0.44	0.22	1.0	0.594	0.512	0.30	0.54	81	0.44	370
1657−261	2015-06-20	0.44	0.16	−7.0	1.122	1.080	1.30	1.13	27	1.04	406
1659+399	2015-06-20	0.46	0.17	2.6	0.103	0.075	0.17	0.11	33	0.05	420
1716+686	2016-04-22	0.49	0.18	2.9	0.232	0.100	0.22	0.24	29	0.05	320
1725+044	2016-02-09	0.54	0.20	18.4	0.421	0.290	0.46	0.41	76	0.27	293
1726+455	2016-02-09	0.44	0.22	3.0	0.887	0.526	0.21	0.88	83	0.33	360
1800+440	2016-02-09	0.43	0.21	8.2	1.025	0.807	0.55	1.02	33	0.54	356
1806+456	2016-04-22	0.51	0.15	12.8	0.389	0.279	0.45	0.39	31	0.16	415
1807+698	2016-04-22	0.52	0.16	16.8	0.887	0.541	1.30	0.83	29	0.54	320
1842+681	2016-02-09	0.46	0.22	6.5	0.179	0.126	0.25	0.18	30	0.12	350
1849+670	2016-02-09	0.48	0.23	3.2	1.449	1.250	0.89	1.45	30	1.03	350
1920−211	2016-04-22	0.44	0.16	−8.9	1.099	0.958	0.24	1.09	27	0.78	430
1926+611	2016-04-22	0.50	0.16	4.8	0.488	0.224	0.26	0.48	30	0.29	460
1957−135	2016-01-18	0.42	0.17	2.3	1.605	1.360	0.80	1.56	26	1.15	408
1958−179	2016-01-18	0.40	0.16	−0.8	2.830	2.230	0.59	2.45	25	1.82	412
2007+777	2016-04-22	0.49	0.17	15.6	0.703	0.440	0.37	0.66	28	0.26	356
2021+317	2016-01-18	0.50	0.17	8.5	0.892	0.443	0.51	0.83	33	0.35	425
2021+614	2016-04-22	0.51	0.19	11.7	0.578	0.193	0.60	0.49	29	0.04	375
2022−077	2016-01-18	0.43	0.17	2.5	1.548	1.430	0.45	1.54	27	1.22	415
2023+335	2016-01-18	0.48	0.17	8.1	1.113	0.762	0.50	1.12	33	0.75	426
2029+121	2016-04-22	0.43	0.16	−5.0	0.546	0.347	0.48	0.54	30	0.31	414
2126−158	2016-01-18	0.47	0.18	4.6	0.359	0.219	0.35	0.36	29	0.26	375
2134+004	2016-04-22	0.75	0.15	−19.0	2.294	0.779	1.50	1.55	32	0.79	260
2135+508	2016-01-18	0.52	0.17	17.5	0.189	0.163	0.11	0.17	30	0.14	445

Table 3—Continued

IAU Name (1)	Observation yyyy-mm-dd (2)	B_{maj} (mas) (3)	B_{min} (mas) (4)	$B_{\text{P.A.}}$ ($^{\circ}$) (5)	S_{tot} (Jy) (6)	S_{peak} (Jy beam $^{-1}$) (7)	σ (mJy beam $^{-1}$) (8)	S_{S} (Jy) (9)	B_{S} (M λ) (10)	S_{L} (Jy) (11)	B_{L} (M λ) (12)
2141+175	2016-04-22	0.41	0.16	2.1	0.546	0.344	0.48	0.44	33	0.26	404
2142+110	2016-04-22	0.43	0.16	−9.1	0.219	0.183	0.35	0.23	28	0.18	400
2144+092	2016-01-18	0.46	0.18	8.4	0.762	0.604	0.17	0.76	32	0.56	406
2155−152	2016-04-22	0.62	0.17	−11.4	1.856	1.100	2.70	1.80	22	0.59	402
2201+171	2016-01-18	0.45	0.18	12.2	0.849	0.805	0.43	0.85	33	0.74	426
2209+236	2016-01-18	0.47	0.18	14.8	0.482	0.244	0.29	0.48	20	0.09	425
2216−038	2016-01-18	0.43	0.17	2.7	0.900	0.574	0.43	0.80	28	0.50	408
2223+210	2016-04-22	0.47	0.16	−6.0	0.475	0.300	0.33	0.48	30	0.29	412
2227−088	2016-01-18	0.44	0.17	2.5	2.732	2.590	1.25	2.73	27	2.26	410
2234+282	2016-01-18	0.51	0.17	0.1	1.139	0.871	0.70	1.09	33	0.82	385
2243−123	2016-01-18	0.42	0.17	3.0	1.673	1.190	0.86	1.62	26	0.29	412
2308+341	2016-01-18	0.51	0.18	−6.8	0.440	0.346	0.50	0.41	33	0.29	395
2318+049	2016-01-18	0.47	0.19	−4.3	0.548	0.333	0.20	0.54	26	0.24	397
2320−035	2016-01-18	0.44	0.18	−0.1	1.049	0.739	0.57	1.04	22	0.74	412
2325+093	2016-01-18	0.46	0.18	−3.8	2.019	1.850	0.45	2.02	26	1.70	409
2342−161	2016-01-18	0.44	0.18	3.2	1.393	1.190	0.70	1.40	18	0.84	420
2344+092	2016-01-18	0.47	0.21	0.9	0.124	0.084	0.42	0.12	26	0.06	410
2345−167	2016-01-18	0.47	0.18	−0.6	2.026	1.470	0.37	2.03	17	1.18	376
2351−154	2016-01-19	0.44	0.18	0.7	0.355	0.182	0.38	0.35	17	0.12	420

Note. — (1) Source name (B1950.0); (2) Observing date; (3) Major axis of the restoring beam (FWHM); (4) Minor axis of the restoring beam (FWHM); (5) Position angle of the major axis, measured from north through east; (6) Integrated flux density; (7) Peak specific intensity; (8) Off-source rms noise in the clean image; (9) Correlated flux density on the shortest baseline; (10) Shortest baseline length in million wavelengths; (11) Correlated flux density on the longest baseline; (12) Longest baseline length in million wavelengths.

Table 4. Model Fit Parameters of Sources

IAU Name (1)	Session (2)	Comp. (3)	S_{tot} (Jy) (4)	S_{peak} Jy beam ⁻¹ (5)	R (mas) (6)	P.A. (°) (7)	d (mas) (8)	T_b (10 ¹⁰ K) (9)
0048–071...	C	C	0.424	0.412	0.05	33.1
		J3	0.028	0.024	0.43	–39.97	0.13	
		J2	0.021	0.014	0.90	–52.83	0.21	
		J1	0.007	0.002	2.36	–57.45	0.53	
0106+013...	B	C	0.869	0.801	0.05	70.7
		J2	0.118	0.103	0.35	–116.37	0.10	
		J1	0.215	0.036	1.36	–136.52	1.04	
0113–118...	C	C	0.657	0.569	0.12	5.0
		J1	0.041	0.011	0.35	–48.46	0.44	
0119+041...	C	C	0.480	0.345	0.18	1.6
		J2	0.048	0.022	1.11	85.24	0.34	
		J1	0.018	0.005	1.57	93.71	0.76	
0122–003...	C	C	0.225	0.256	0.05	12.3
		J3	0.162	0.149	0.17	–99.15	0.18	
		J2	0.016	0.004	0.99	–98.53	0.50	
		J1	0.022	0.005	2.37	–93.12	0.61	
0130–171...	B	C	0.438	0.391	0.08	9.1
		J2	0.084	0.015	0.34	–110.92	0.57	
		J1	0.075	0.018	1.01	–108.83	0.47	
0149+218...	C	C	1.071	0.969	0.09	20.1
		J1	0.089	0.198	0.42	–6.17	0.13	
0202–172...	C	C	0.757	0.676	0.10	13.6
		J4	0.101	0.055	0.88	–6.04	0.27	
		J3	0.061	0.011	2.75	4.99	0.73	
		J2	0.035	0.038	4.37	–0.73	<0.12	
		J1	0.061	0.045	4.76	2.87	0.17	
0208+106...	C	C	0.325	0.314	0.06	7.1
		J3	0.138	0.111	0.35	125.01	0.15	
		J2	0.019	0.006	0.76	104.84	0.56	
		J1	0.048	0.008	1.43	49.64	1.54	
0221+067...	B	C	0.911	0.696	0.06	25.1
		J2	0.077	0.279	0.23	–76.07	0.20	
		J1	0.032	0.020	1.21	–78.87	1.36	
0224+671...	C	C	0.352	0.294	0.13	2.1
		J1	0.166	0.106	0.67	10.41	0.22	

Table 4—Continued

IAU Name (1)	Session (2)	Comp. (3)	S_{tot} (Jy) (4)	S_{peak} Jy beam $^{-1}$ (5)	R (mas) (6)	P.A. ($^{\circ}$) (7)	d (mas) (8)	T_b (10^{10}K) (9)
0229+131...	C	C	0.460	0.442	0.07	18.8
		J1	0.232	0.101	0.84	63.58	0.40	
0239+108...	C	C	0.215	0.189	0.14	2.6
		J2	0.018	0.019	0.51	117.76	<0.12	
		J1	0.007	0.004	2.83	137.52	0.36	
0241+622...	C	C	0.802	0.693	0.13	3.3
		J1	0.023	0.016	0.54	99.16	0.22	
		JW	0.007	0.006	0.55	−100.79	<0.12	
0306+102...	C	C	0.882	0.776	0.12	7.5
		J1	0.017	0.016	0.73	60.58	0.11	
0309+411...	B	C	0.331	0.388	0.06	6.9
		J4	0.218	0.353	0.14	−57.36	0.10	
		J3	0.111	0.261	0.23	−55.18	0.11	
		J2	0.064	0.082	0.42	−54.16	0.29	
		J1	0.011	0.008	0.84	−56.88	0.22	
0322+222...	C	C	0.509	0.487	0.08	16.1
		J2	0.032	0.158	0.24	128.47	0.26	
		J1	0.012	0.006	1.06	90.61	0.50	
0354+559...	B	C	0.202	0.211	0.05	10.6
		J2	0.155	0.107	0.22	−67.95	0.18	
		J1	0.164	0.042	0.42	−140.71	0.35	
0400+258...	C	C	0.175	0.112	0.21	0.8
		J2	0.051	0.019	0.95	87.28	0.39	
		J1	0.011	0.009	1.43	103.90	0.16	
0403−132...	C	C	0.300	0.281	0.10	3.1
		J2	0.026	0.025	2.53	149.29	<0.13	
		J1	0.011	0.011	3.17	149.86	<0.14	
0405−123...	B	C	0.434	0.389	0.06	12.4
		J1	0.367	0.285	0.50	11.98	0.10	
0420+417...	C	C	0.266	0.222	0.14	1.8
		J1	0.034	0.034	0.56	−97.76	<0.15	
0451−282...	B	C	0.764	0.741	0.05	71.4
		J2	0.182	0.097	0.57	−1.95	0.33	
		J1	0.012	0.011	1.96	−7.53	0.08	
0507+179...	C	C	2.464	2.440	0.03	254.4

Table 4—Continued

IAU Name (1)	Session (2)	Comp. (3)	S_{tot} (Jy) (4)	S_{peak} Jy beam ⁻¹ (5)	R (mas) (6)	P.A. (°) (7)	d (mas) (8)	T_b (10 ¹⁰ K) (9)
0529+075...	C	J1	0.024	0.024	0.61	−105.16	0.31	28.5
		C	1.232	1.042	0.08	
		J2	0.084	0.014	1.24	−8.14	0.89	
0605−085...	B	J1	0.036	0.028	1.92	−10.21	0.26	4.7
		C	0.622	0.464	0.08	
		J2	1.356	0.639	0.44	81.08	0.16	
0627−199...	B	J1	0.069	0.075	0.77	119.99	0.11	25.7
		C	0.359	0.341	0.05	
		J1	0.064	0.049	0.41	25.26	0.13	
0633+734...	C	C	0.386	0.381	0.05	28.9
		J2	0.018	0.081	0.45	−11.51	0.17	
		J1	0.007	0.006	1.62	−5.61	0.14	
0648−165...	C	C	0.343	0.352	0.06	12.5
		J2	0.106	0.087	0.48	−3.07	0.54	
		J1	0.052	0.011	0.83	−67.81	0.94	
0657+172...	B	C	0.202	0.184	0.09	3.3
		J1	0.133	0.031	0.38	−61.04	0.47	
		C	0.344	0.330	0.07	
0708+506...	B	J1	0.026	0.054	0.20	99.33	0.22	6.9
		C	0.651	0.558	0.09	
		J3	0.104	0.084	0.48	−40.07	0.12	
0723−008...	B	J2	0.344	0.105	1.75	−39.71	0.41	5.7
		J1	0.672	0.152	2.65	−34.62	0.51	
		C	0.189	0.127	0.08	
0730+504...	C	J1	0.026	0.007	1.03	−139.55	0.42	3.3
		C	0.680	0.424	0.18	
		J1	0.026	0.023	0.41	−42.26	<0.12	
0736+017...	C	C	0.497	0.467	0.07	10.9
		J3	0.201	0.226	0.45	177.20	0.09	
		J2	0.101	0.111	0.83	−178.13	0.14	
0738+313...	C	J1	0.343	0.059	3.47	174.32	0.43	8.4
		C	0.286	0.257	0.09	
		J2	0.101	0.005	2.18	−9.50	1.75	
0742+103...	C	J1	0.025	0.008	3.04	−34.22	0.49	3.1
		C	0.190	0.177	0.09	
		J1	0.025	0.008	3.04	−34.22	0.49	
0743−006...	C	C	0.190	0.177	0.09	3.1
		J1	0.025	0.008	3.04	−34.22	0.49	
		C	0.190	0.177	0.09	

Table 4—Continued

IAU Name (1)	Session (2)	Comp. (3)	S_{tot} (Jy) (4)	S_{peak} Jy beam ⁻¹ (5)	R (mas) (6)	P.A. (°) (7)	d (mas) (8)	T_b (10 ¹⁰ K) (9)
		J4	0.071	0.066	0.21	46.52	0.35	
		J3	0.095	0.071	0.91	57.87	0.15	
		J2	0.038	0.044	1.14	52.67	0.21	
		J1	0.097	0.048	1.46	48.98	0.25	
0754+100...	C	C	0.387	0.480	<0.04	>20.1
		J4	0.151	0.401	0.18	4.23	0.07	
		J3	0.080	0.151	0.40	9.19	0.16	
		J2	0.039	0.023	1.38	16.62	0.20	
		J1	0.012	0.009	1.79	16.86	0.26	
0805+410...	C	C	0.844	0.643	0.18	4.1
0805–077...	B	C	0.554	0.534	0.05	41.3
		J1	0.051	0.141	0.39	–11.74	0.11	
0808+019...	C	C	1.152	1.106	0.05	101.5
		J2	0.013	0.041	0.53	–174.60	<0.11	
		J1	0.010	0.011	0.74	–165.27	<0.12	
0821+394...	C	C	0.283	0.206	0.12	2.9
		J2	0.028	0.050	0.34	–54.69	0.28	
		J1	0.009	0.002	1.09	–52.76	0.64	
0838+133...	C	C	0.552	0.436	0.12	4.2
		J2	0.113	0.024	0.32	93.04	0.51	
		J1	0.046	0.018	0.97	98.55	0.30	
0847–120...	C	C	0.837	0.743	0.08	13.4
0859–140...	C	C	0.092	0.086	0.10	1.4
		J3	0.036	0.055	0.23	130.41	0.09	
		J2	0.020	0.011	0.86	139.42	0.23	
		J1	0.050	0.010	1.73	152.31	0.57	
0906+015...	C	C	0.437	0.402	0.08	9.1
		J3	0.207	0.141	0.38	44.18	0.17	
		J2	0.113	0.059	0.85	45.91	0.24	
		J1	0.032	0.007	1.63	41.81	0.47	
0917+624...	C	C	0.451	0.420	0.05	29.0
		J4	0.028	0.026	0.55	–31.91	0.17	
		J3	0.026	0.015	1.05	–36.22	0.19	
		J2	0.013	0.007	1.39	–49.29	0.23	
		J1	0.054	0.011	2.03	–40.78	0.54	

Table 4—Continued

IAU Name (1)	Session (2)	Comp. (3)	S_{tot} (Jy) (4)	S_{peak} Jy beam $^{-1}$ (5)	R (mas) (6)	P.A. ($^{\circ}$) (7)	d (mas) (8)	T_b (10^{10}K) (9)
0925–203...	B	C	0.257	0.249	0.05	9.1
		J1	0.113	0.058	0.87	–30.23	0.21	
0945+408...	B	C	0.227	0.152	0.15	1.5
		J3	0.014	0.011	0.52	96.89	0.11	
		J2	0.013	0.007	1.10	104.19	0.27	
		J1	0.054	0.011	1.61	110.17	0.55	
1032–199...	B	C	0.236	0.233	0.05	19.8
		J2	0.051	0.032	0.49	–141.11	0.18	
		J1	0.048	0.008	1.12	–142.63	0.58	
1036+054...	C	C	0.072	0.070	<0.04	>4.3
		J3	0.197	0.199	0.60	–19.61	0.05	
		J2	0.029	0.114	0.85	–14.21	0.15	
		J1	0.034	0.019	1.78	–15.38	0.22	
1038+064...	C	C	0.363	0.326	0.08	8.4
		J1	0.018	0.007	1.42	178.29	0.36	
1045–188...	C	C	0.152	0.126	0.12	1.1
		J1	0.586	0.422	0.75	157.72	0.21	
1049+215...	C	C	0.246	0.128	0.22	0.8
1124–186...		C	1.238	1.10	0.21	3.8
		J1	0.031	0.103	0.64	160.97	0.41	
1149–084...	B	C	0.185	0.126	0.16	1.6
		J1	0.141	0.107	0.29	109.53	0.14	
1150+497...	B	C	0.661	0.617	0.09	7.1
		J4	0.059	0.155	0.46	–163.18	0.15	
		J3	0.078	0.054	0.91	–151.19	0.16	
		J2	0.028	0.013	1.55	–152.13	0.28	
		J1	0.011	0.010	1.91	–157.46	0.18	
1213–172...	C	C	0.357	0.155	0.35	0.4
		J1	0.203	0.077	0.48	80.74	0.27	
1219+044...	B	C	0.622	0.563	0.10	8.1
		J1	0.006	0.006	0.64	–179.81	0.05	
1228+126...	B	C	0.724	0.604	0.13	2.8
		J4	0.148	0.291	0.19	–52.42	0.24	
		J3	0.202	0.033	0.54	–89.42	0.62	
		J2	0.069	0.016	1.30	–51.87	0.54	

Table 4—Continued

IAU Name (1)	Session (2)	Comp. (3)	S_{tot} (Jy) (4)	S_{peak} Jy beam ⁻¹ (5)	R (mas) (6)	P.A. (°) (7)	d (mas) (8)	T_b (10 ¹⁰ K) (9)
		J1	0.188	0.006	1.74	−91.03	1.82	
1243−072...	C	C	0.731	0.754	0.05	43.9
		J1	0.197	0.162	0.28	−121.06	0.47	
1257+519...	B	C	0.308	0.289	0.09	3.5
		J1	0.031	0.110	0.16	−108.9	0.11	
1306+360...	B	C	0.653	0.625	0.08	13.8
		J1	0.016	0.027	0.46	−11.64	0.12	
1324+224...	C	C	0.295	0.281	0.06	12.9
		J1	0.019	0.004	0.61	−60.96	0.69	
1329−049...	B	C	0.811	0.557	0.14	8.6
1354+195...	C	C	0.671	0.583	0.11	6.3
		J2	0.451	0.307	0.43	115.69	0.19	
		J1	0.132	0.033	1.41	128.88	0.44	
1417+385...	C	C	0.172	0.145	0.16	1.2
1435+638...	C	C	0.108	0.095	0.08	0.8
		J1	0.159	0.101	1.72	−128.04	0.20	
1502+106...	C	C	2.827	2.766	0.06	146.2
		J1	0.082	0.011	0.51	118.79	0.08	
1504−166...	C	C	0.537	0.511	0.07	13.5
		J2	0.012	0.189	0.52	−174.56	0.28	
		J1	0.004	0.003	1.93	177.99	0.33	
1514+004...	C	C	0.348	0.299	0.12	1.7
		J1	0.081	0.059	0.66	−30.51	0.18	
1514+197...	C	C	0.617	0.501	0.11	6.9
		J1	0.011	0.002	1.09	−17.81	0.67	
1532+016...	C	C	0.304	0.223	0.16	1.9
		J1	0.115	0.019	0.95	−129.83	0.69	
1546+027...	C	C	2.485	2.061	0.15	10.2
		J1	0.031	0.011	1.02	−176.68	0.45	
1548+056...	B	C	0.558	0.448	0.08	13.8
		J3	0.188	0.103	1.21	−7.89	0.23	
		J2	0.205	0.031	2.06	−6.35	0.66	
		J1	0.105	0.007	3.06	7.41	1.06	
1606+106...	C	C	0.523	0.496	0.07	15.6
		J1	0.026	0.002	1.06	−52.14	1.01	

Table 4—Continued

IAU Name (1)	Session (2)	Comp. (3)	S_{tot} (Jy) (4)	S_{peak} Jy beam $^{-1}$ (5)	R (mas) (6)	P.A. ($^{\circ}$) (7)	d (mas) (8)	T_b (10^{10}K) (9)
1636+473...	C	C	0.445	0.374	0.08	7.9
		J1	0.017	0.005	1.11	−11.66	0.47	
1637+826...	C	C	0.365	0.258	0.17	0.8
		J2	0.036	0.036	0.41	−72.25	0.29	
		J1	0.031	0.014	0.92	−64.21	0.41	
1639−062...	C	C	0.677	0.628	0.09	13.6
		J1	0.032	0.005	0.41	101.62	0.80	
1642+690...	B	C	0.592	0.489	0.13	4.1
		J1	0.188	0.108	1.21	−158.27	0.25	
1655+077...	C	C	0.393	0.348	0.11	3.5
		J1	0.087	0.026	0.55	−46.81	0.35	
1656+477...	C	C	0.558	0.512	0.11	7.9
		J2	0.013	0.021	0.63	0.49	0.24	
		J1	0.023	0.011	1.44	−1.21	0.30	
1657−261...	B	C	1.122	1.079	0.06	40.9
1659+399...	B	C	0.083	0.075	0.08	1.3
		J1	0.020	0.013	0.49	−161.78	0.21	
1716+686...	B	C	0.152	0.100	0.09	2.2
		J2	0.056	0.054	0.49	−21.09	0.19	
		J1	0.024	0.017	0.89	−26.30	0.29	
1725+044...	C	C	0.387	0.290	0.10	3.3
		J1	0.034	0.009	0.45	119.59	0.52	
1726+455...	C	C	0.500	0.526	0.06	15.6
		J1	0.387	0.321	0.31	−137.26	0.21	
1800+440...	C	C	0.742	0.805	0.05	32.4
		J1	0.283	0.404	0.35	−148.77	0.14	
1806+456...	B	C	0.355	0.279	0.12	3.0
		J2	0.028	0.027	0.53	176.89	0.22	
		J1	0.006	0.006	0.96	−173.55	0.29	
1807+698...	B	C	0.623	0.541	0.09	5.3
		J2	0.169	0.066	0.36	−106.82	0.31	
		J1	0.095	0.039	1.14	−105.22	0.30	
1842+681...	C	C	0.130	0.126	0.07	2.6
		J2	0.040	0.046	0.27	133.08	0.07	
		J1	0.009	0.016	0.51	135.84	0.26	

Table 4—Continued

IAU Name (1)	Session (2)	Comp. (3)	S_{tot} (Jy) (4)	S_{peak} Jy beam ⁻¹ (5)	R (mas) (6)	P.A. (°) (7)	d (mas) (8)	T_b (10 ¹⁰ K) (9)
1849+670...	C	C	1.306	1.252	0.06	39.4
		J1	0.143	0.091	0.51	-21.91	0.34	
1920–211...	B	C	1.012	0.958	0.05	49.8
		J2	0.039	0.056	0.49	1.89	0.28	
		J1	0.048	0.002	2.44	-15.52	1.33	
1926+611...	B	C	0.220	0.224	0.05	11.5
		J3	0.189	0.179	0.17	84.83	<0.09	
		J2	0.055	0.017	0.58	118.94	0.18	
		J1	0.024	0.003	1.41	121.81	0.68	
1957–135...	C	C	1.452	1.360	0.13	6.9
		J2	0.083	0.064	1.11	17.79	0.12	
		J1	0.070	0.046	1.67	17.82	0.16	
1958–179...	C	C	2.805	2.233	0.13	18.1
		J1	0.025	0.025	0.44	100.22	<0.12	
2007+777...	B	C	0.569	0.440	0.06	13.9
		J3	0.023	0.013	0.41	-97.44	0.29	
		J2	0.052	0.033	0.81	-103.29	0.19	
		J1	0.059	0.017	1.53	-89.68	0.42	
2021+317...	C	C	0.101	0.086	0.09	0.9
		J5	0.491	0.441	0.41	126.62	0.11	
		J4	0.213	0.196	0.80	-155.18	0.18	
		J3	0.056	0.011	1.65	-160.32	0.56	
		J2	0.020	0.003	2.74	-165.69	0.61	
		J1	0.011	0.011	4.02	-170.19	0.01	
2021+614...	B	C	0.347	0.193	0.25	0.5
		J3	0.129	0.103	0.59	8.00	0.16	
		J2	0.083	0.035	2.01	31.39	0.32	
		J1	0.019	0.011	7.09	31.83	0.18	
2022–077...	C	C	1.479	1.435	<0.04	>144.8
		J2	0.062	0.020	1.01	-13.84	0.35	
		J1	0.007	0.005	2.33	7.67	0.14	
2023+335...	C	C	0.875	0.762	0.11	5.8
		J2	0.178	0.101	0.39	-51.83	0.22	
		J1	0.060	0.021	0.71	-13.03	0.56	
2029+121...	B	C	0.326	0.347	<0.04	>29.6

Table 4—Continued

IAU Name (1)	Session (2)	Comp. (3)	S_{tot} (Jy) (4)	S_{peak} Jy beam ⁻¹ (5)	R (mas) (6)	P.A. (°) (7)	d (mas) (8)	T_b (10 ¹⁰ K) (9)
		J2	0.174	0.174	0.20	−132.37	0.11	
		J1	0.046	0.017	0.81	−159.29	0.32	
2126−158...	C	C	0.317	0.219	0.35	0.7
		J1	0.042	0.028	1.03	−165.82	0.18	
2134+004...	B	C	0.940	0.779	0.11	14.9
		J2	0.412	0.152	0.56	−41.01	0.41	
		J1	0.942	0.149	2.22	−92.78	0.70	
2135+508...	C	C	0.178	0.163	0.76	0.04
		J2	0.004	0.033	0.48	28.04	0.12	
		J1	0.007	0.001	3.49	50.43	0.72	
2141+175...	B	C	0.348	0.344	0.06	7.7
		J2	0.165	0.087	0.19	−91.04	0.24	
		J1	0.033	0.038	0.44	−63.15	0.20	
2142+110...	B	C	0.165	0.183	<0.04	>10.5
		J2	0.038	0.129	0.19	159.96	0.05	
		J1	0.016	0.018	0.57	169.28	0.12	
2144+092...	C	C	0.610	0.604	0.04	52.9
		J2	0.142	0.105	0.27	59.37	0.17	
		J1	0.010	0.003	0.88	67.39	0.33	
2155−152...	B	C	1.715	1.103	0.18	5.8
		J1	0.141	0.139	1.71	−140.30	<0.05	
2201+171...	C	C	0.840	0.805	0.08	17.9
		J1	0.009	0.010	0.56	34.74	<0.10	
2209+236...	C	C	0.265	0.244	0.08	5.9
		J3	0.086	0.104	0.22	86.41	0.13	
		J2	0.110	0.092	0.48	61.73	0.09	
		J1	0.021	0.006	1.48	29.82	0.46	
2216−038...	C	C	0.638	0.573	0.13	4.7
		J2	0.086	0.056	0.62	−161.68	0.17	
		J1	0.176	0.054	1.74	−158.70	0.37	
2223+210...	B	C	0.072	0.033	<0.05	>5.6
		J3	0.036	0.030	0.19	−95.18	0.09	
		J2	0.334	0.072	0.45	−97.74	0.07	
		J1	0.033	0.004	1.37	−115.18	0.72	
2227−088...	C	C	2.711	2.588	0.06	126.5

Table 4—Continued

IAU Name (1)	Session (2)	Comp. (3)	S_{tot} (Jy) (4)	S_{peak} Jy beam $^{-1}$ (5)	R (mas) (6)	P.A. ($^{\circ}$) (7)	d (mas) (8)	T_b (10^{10}K) (9)
2234+282...	C	J1	0.021	0.018	1.70	−3.83	0.08	
		C	0.850	0.870	<0.04	>39.9
		J2	0.110	0.270	0.15	58.54	0.12	
2243−123...	C	J1	0.179	0.061	0.86	39.06	0.34	
		C	1.599	1.185	0.28	2.2
		J2	0.036	0.044	0.71	5.02	0.05	
2308+341...	C	J1	0.038	0.012	3.43	9.09	0.38	
		C	0.374	0.345	0.31	0.7
		J3	0.042	0.058	0.54	−4.44	0.24	
		J2	0.007	0.008	0.61	26.79	0.09	
2318+049...	C	J1	0.017	0.007	1.96	−0.44	0.31	
		C	0.487	0.330	0.16	2.1
2320−035...	C	J1	0.061	0.053	0.34	−46.28	0.49	
		C	0.982	0.737	0.18	4.8
2325+093...	C	J1	0.067	0.004	1.91	−27.87	1.09	
		C	2.019	1.851	0.11	31.1
2342−161...	C	C	1.393	1.185	0.17	5.1
2344+092...	C	C	0.105	0.084	0.14	0.6
		J1	0.019	0.012	1.31	39.55	0.21	
2345−167...	C	C	1.822	1.472	0.18	5.8
		J2	0.051	0.039	0.57	91.98	0.14	
		J1	0.153	0.051	1.83	120.24	0.38	
2351−154...	C	C	0.217	0.182	0.18	1.6
		J3	0.098	0.063	0.47	−63.63	0.18	
		J2	0.029	0.007	1.12	−34.04	0.51	
		J1	0.011	0.003	2.68	−25.95	0.46	

Note. — (1) Source name (B1950.0); (2) Observing session; (3) Component label; (4) Integrated flux density of the fitted Gaussian model component; (5) Peak intensity; (5) Distance from the core; (8) Position angle with respect to the core, measured from north through east; (9) Core brightness temperature.

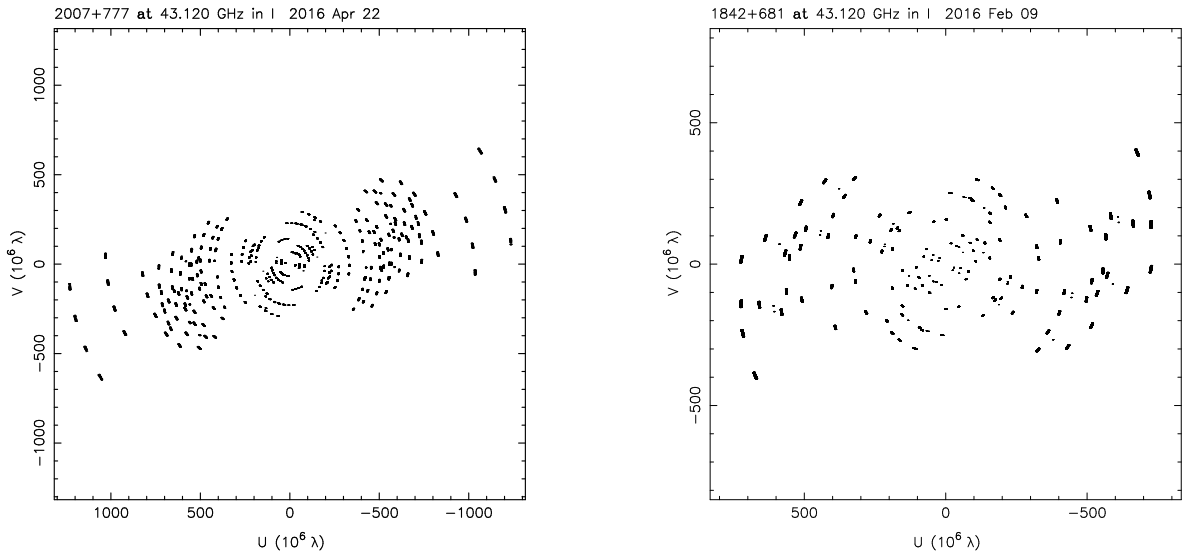


Fig. 1.— Example (u, v) coverages at 43 GHz for a source in the first sample (left panel) and in the second sample (right panel). The labels on the vertical and horizontal axes are in units of million times the observing wavelength (λ).

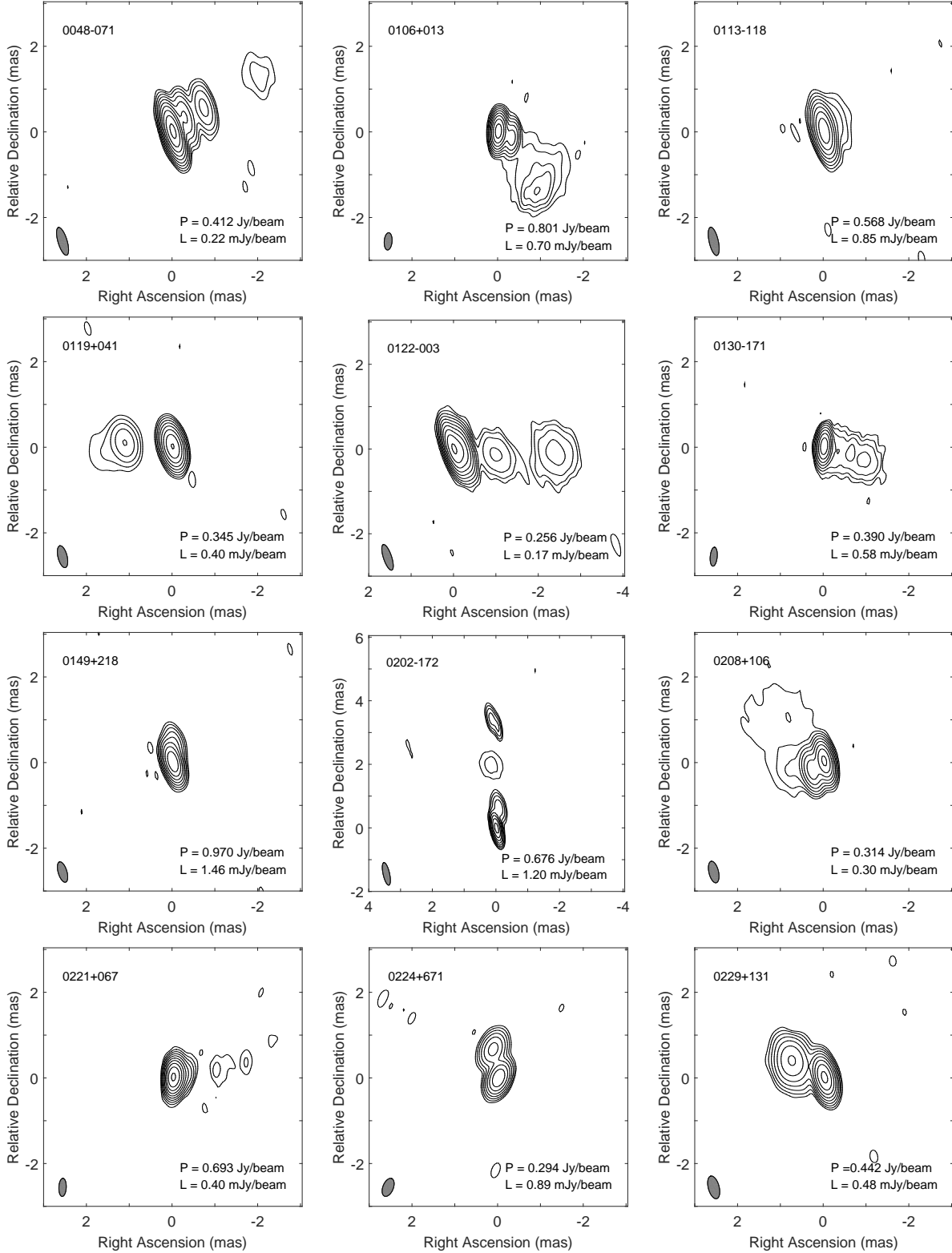


Fig. 2.— Naturally weighted total intensity VLBA images of 124 sources at 43 GHz. The legends in the image: P – peak intensity (in units of Jy beam^{-1}); L – rms noise (in units of mJy beam^{-1}). The lowest contours are at ± 3 times rms noise and further positive contours are drawn at increasing steps of 2. The image parameters are given in Table 3. The gray ellipse in the lower left corner of each image is the restoring beam.

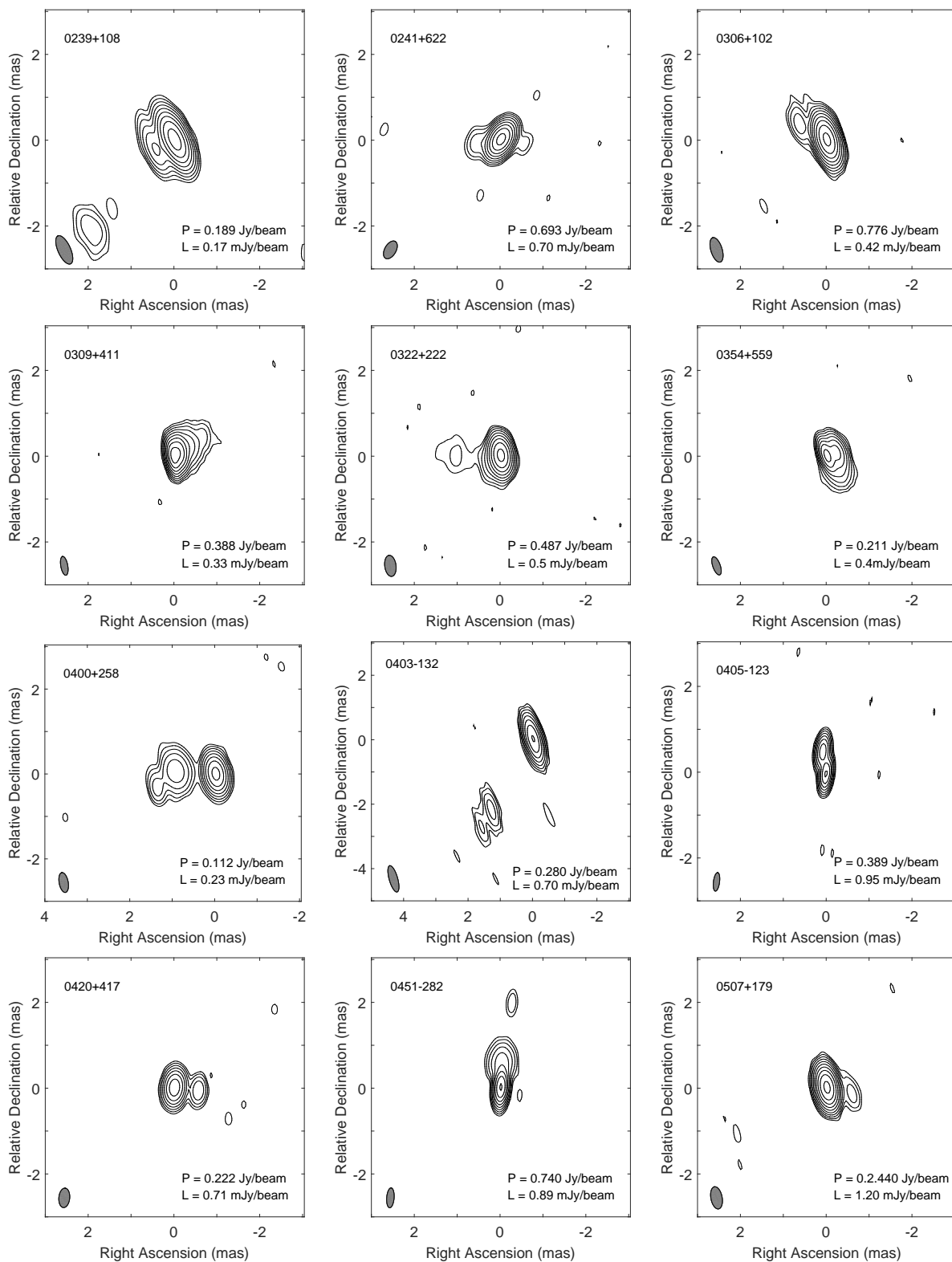


Fig. 3.— VLBA images — Continued

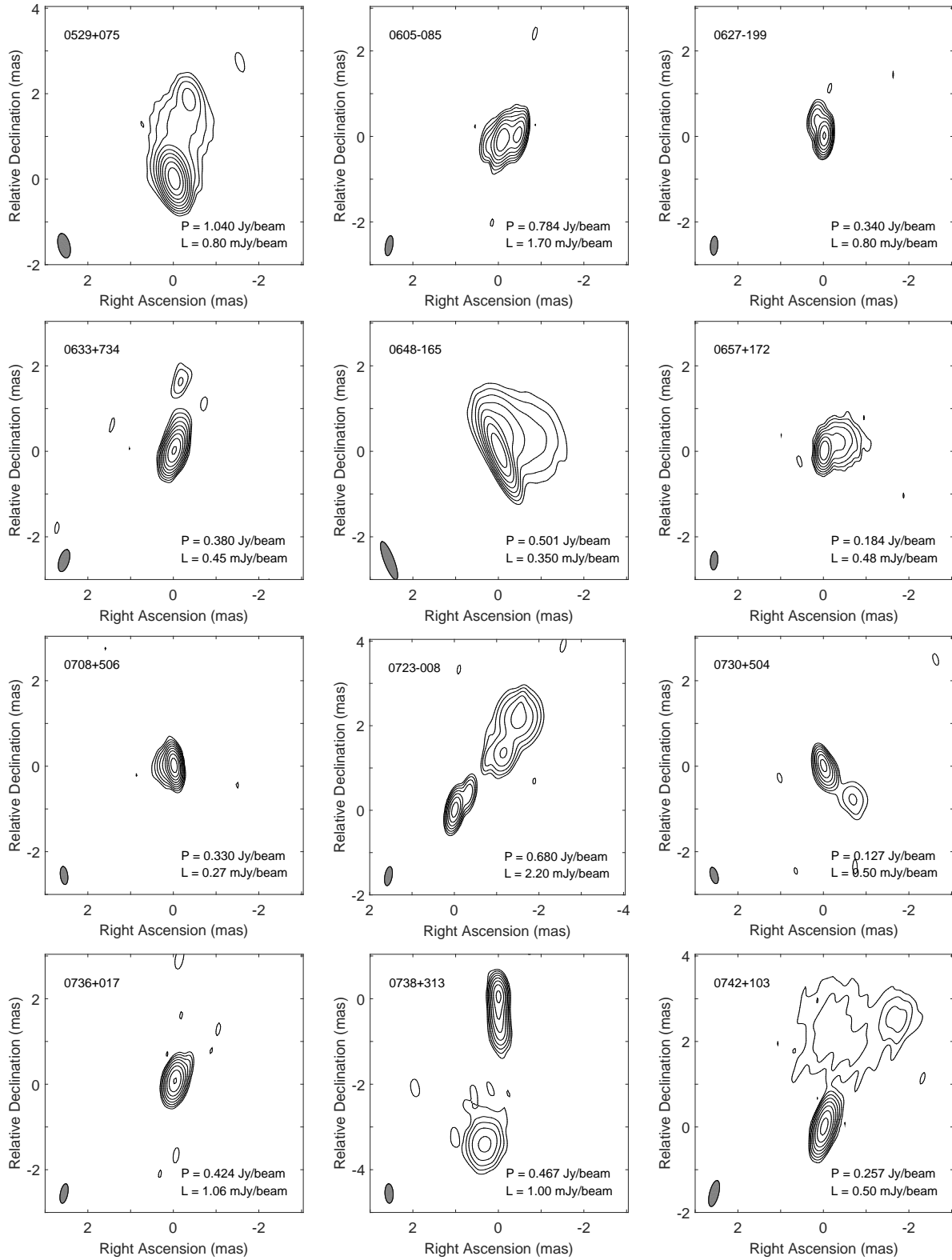


Fig. 4.— VLBA images — Continued

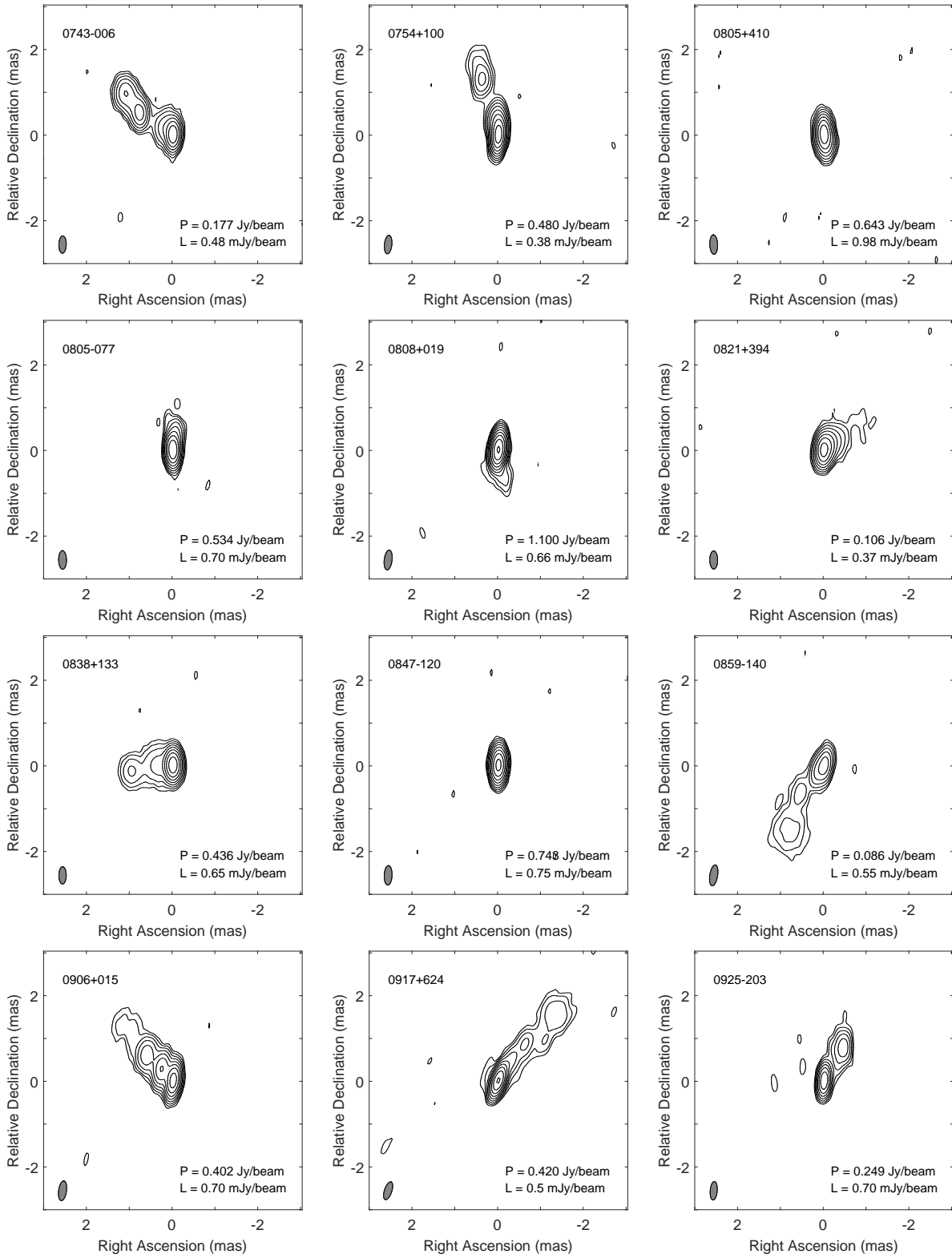


Fig. 5.— VLBA images — Continued

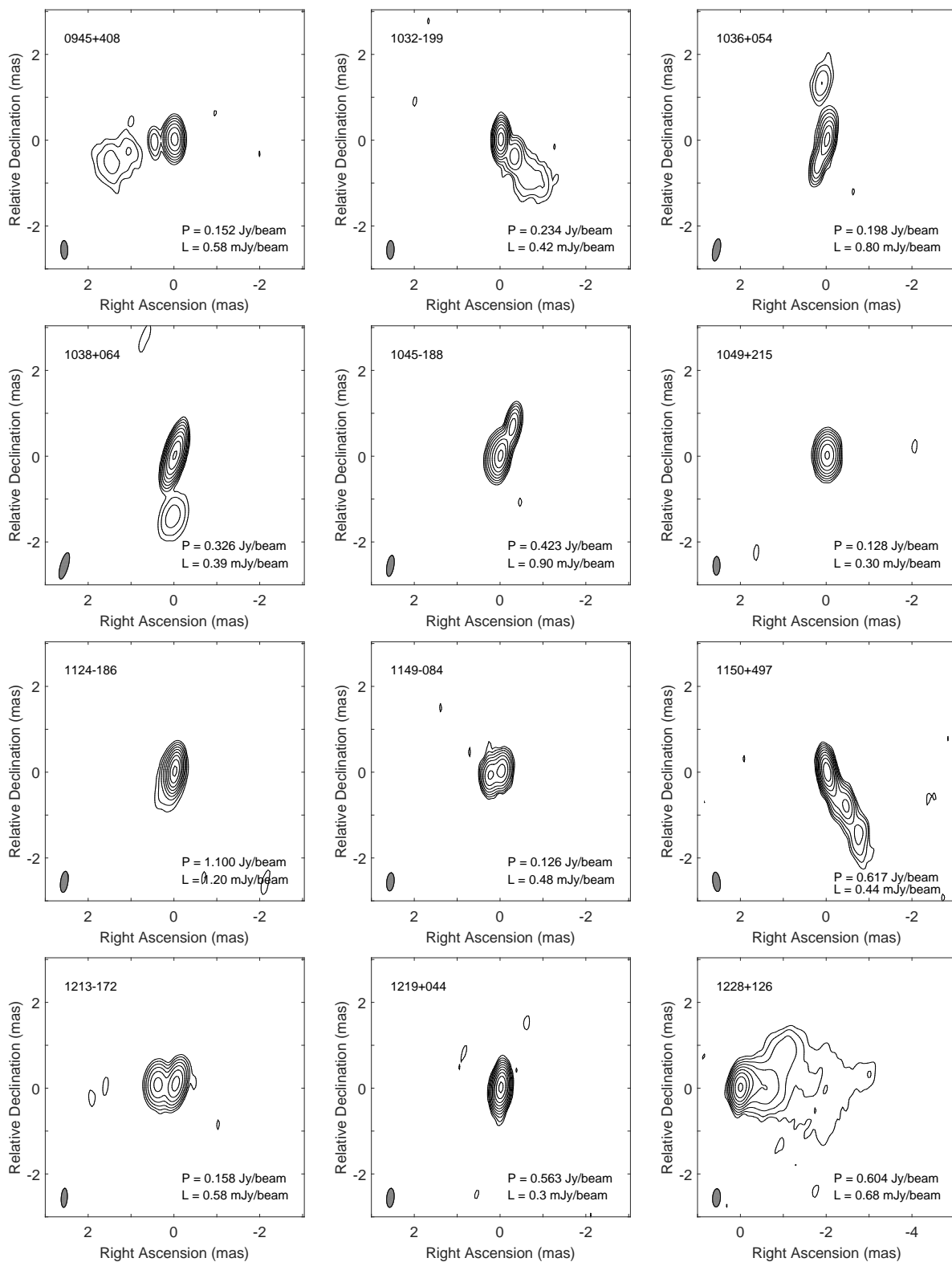


Fig. 6.— VLBA images — Continued

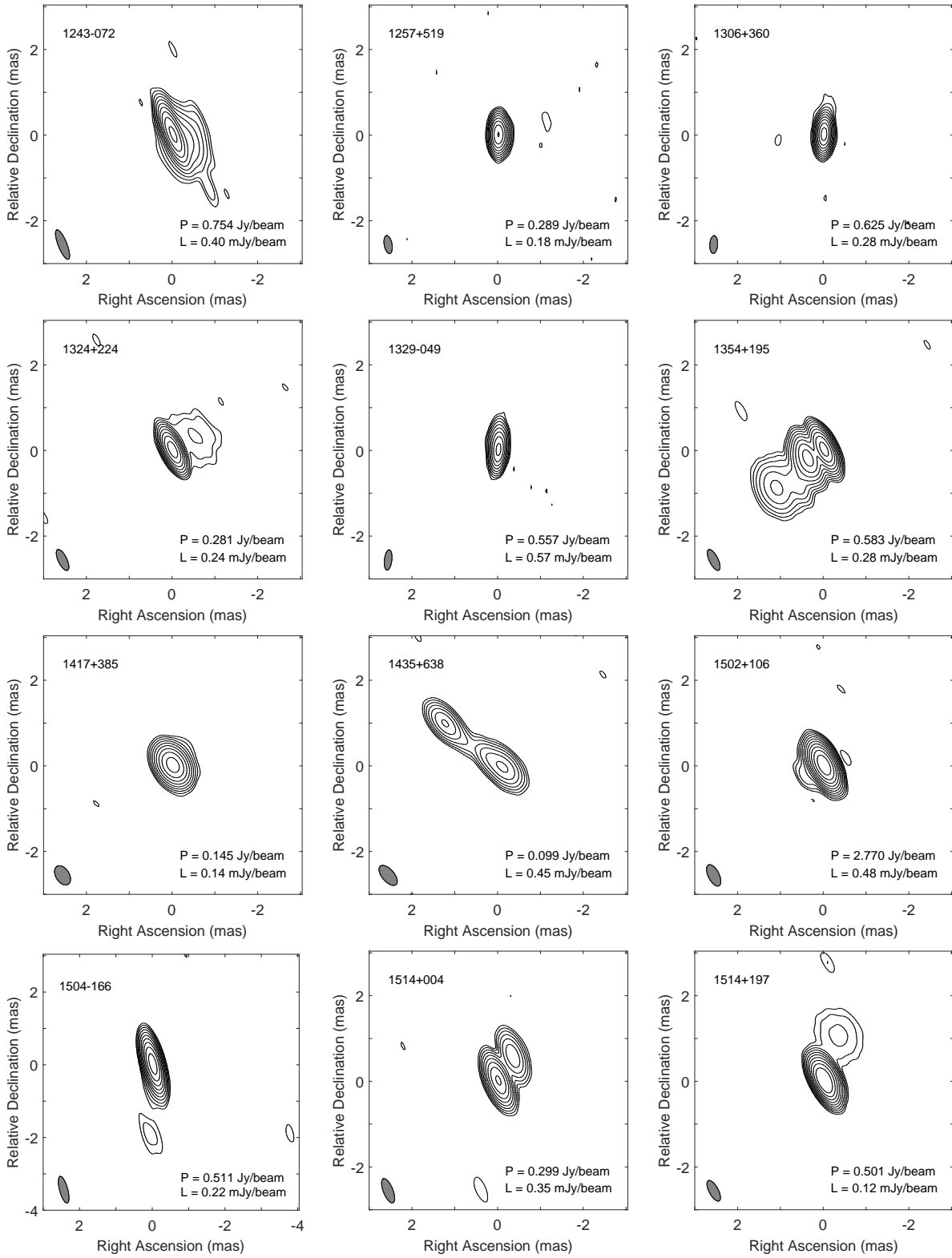


Fig. 7.— VLBA images — Continued

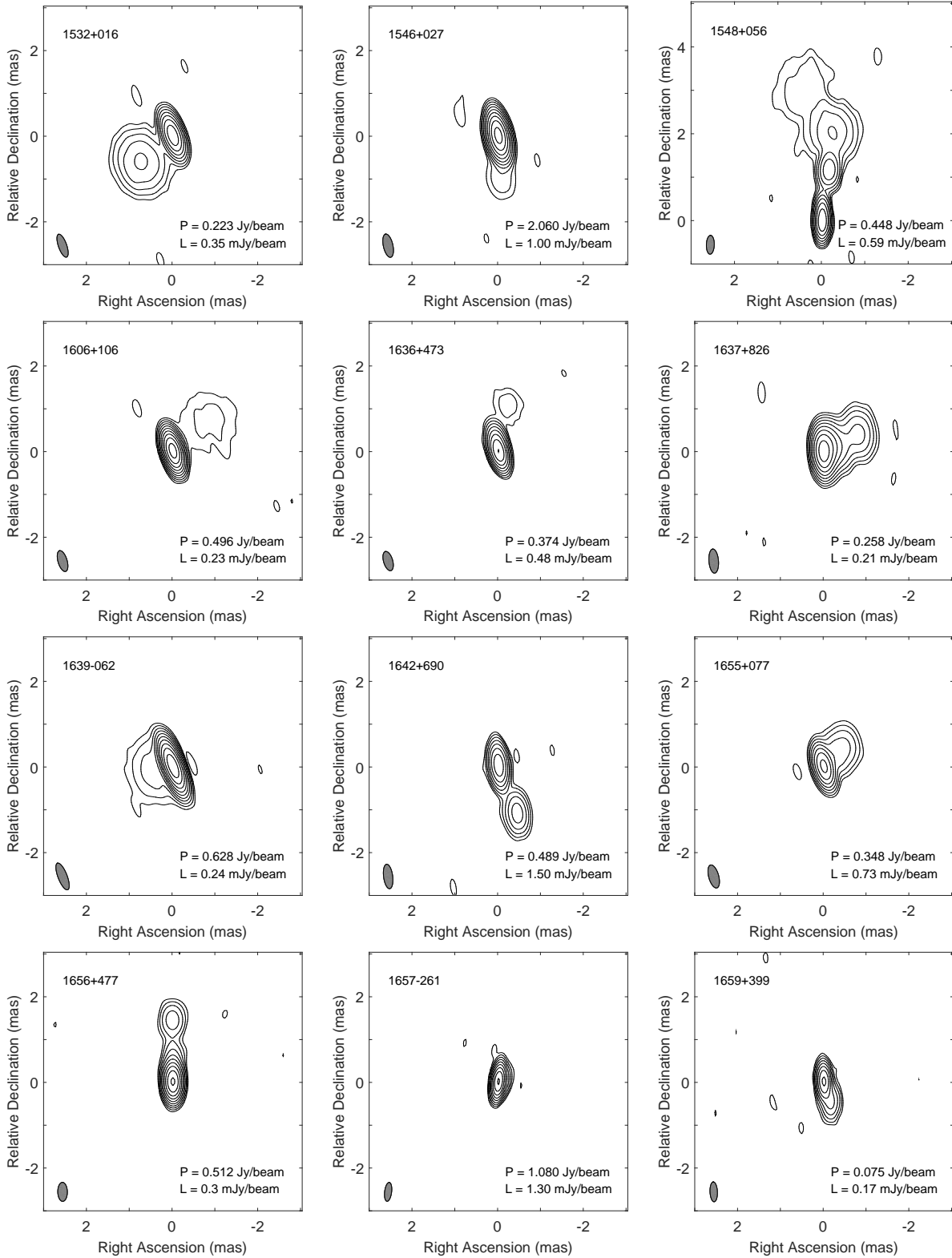


Fig. 8.— VLBA images — Continued

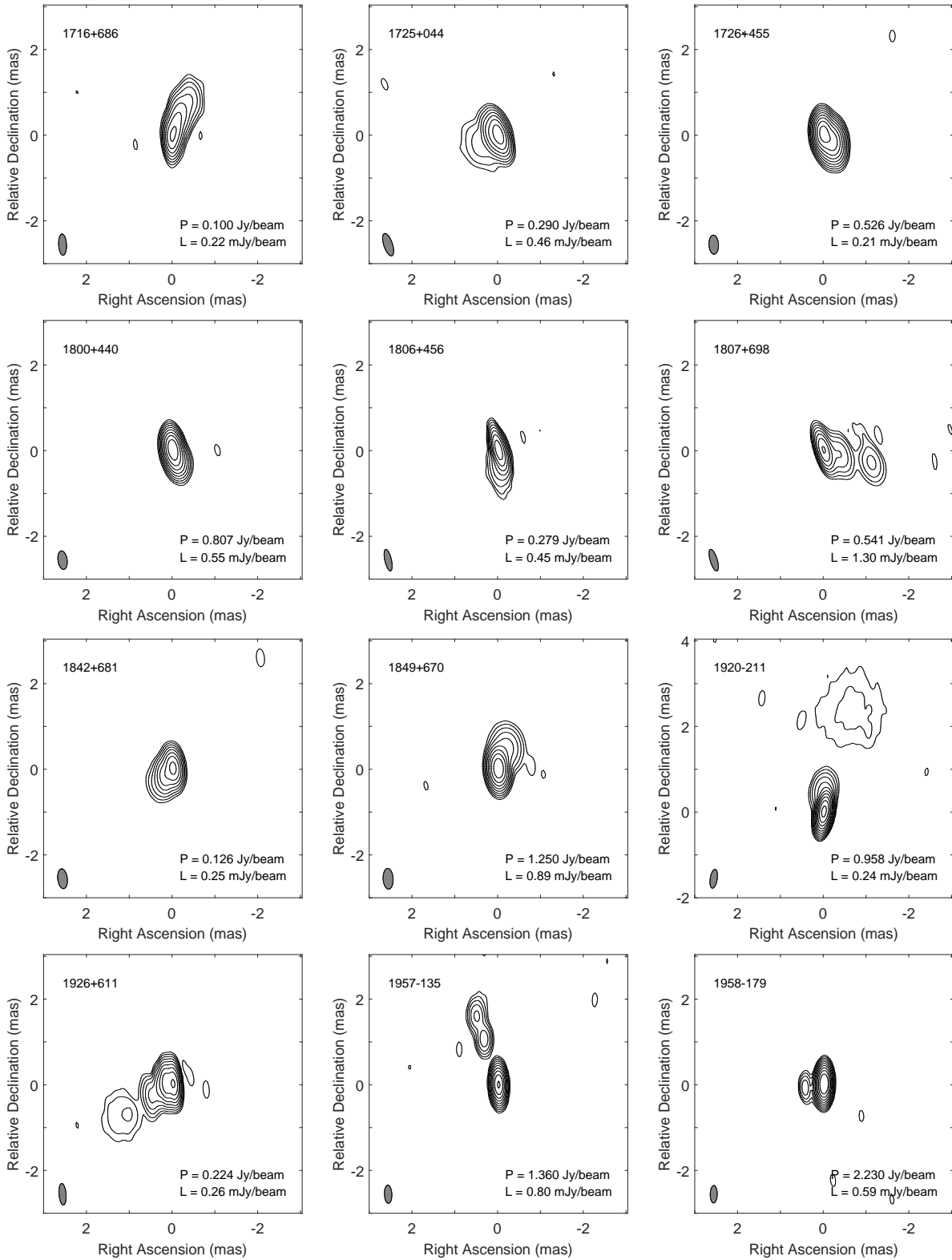


Fig. 9.— VLBA images — Continued

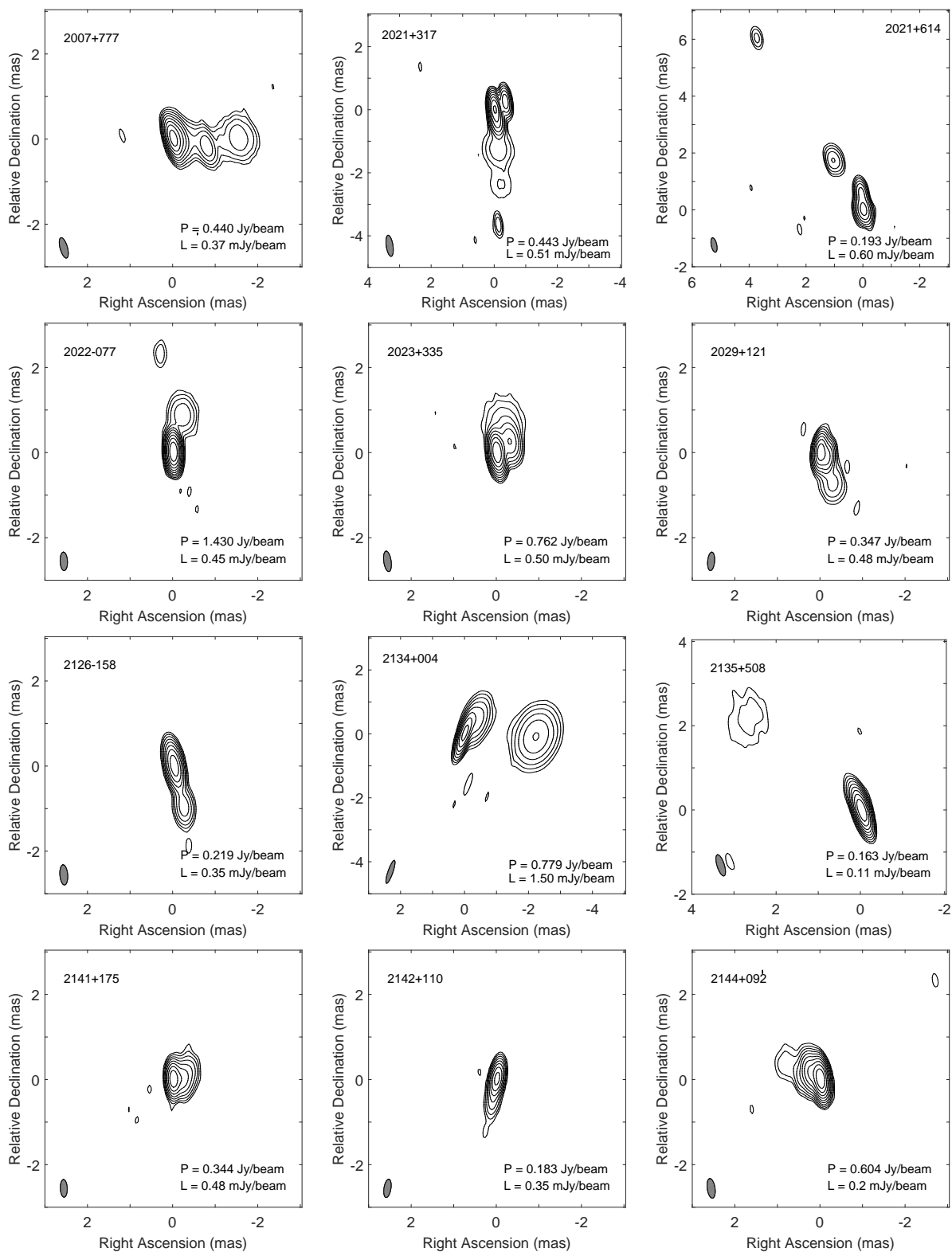


Fig. 10.— VLBA images — Continued

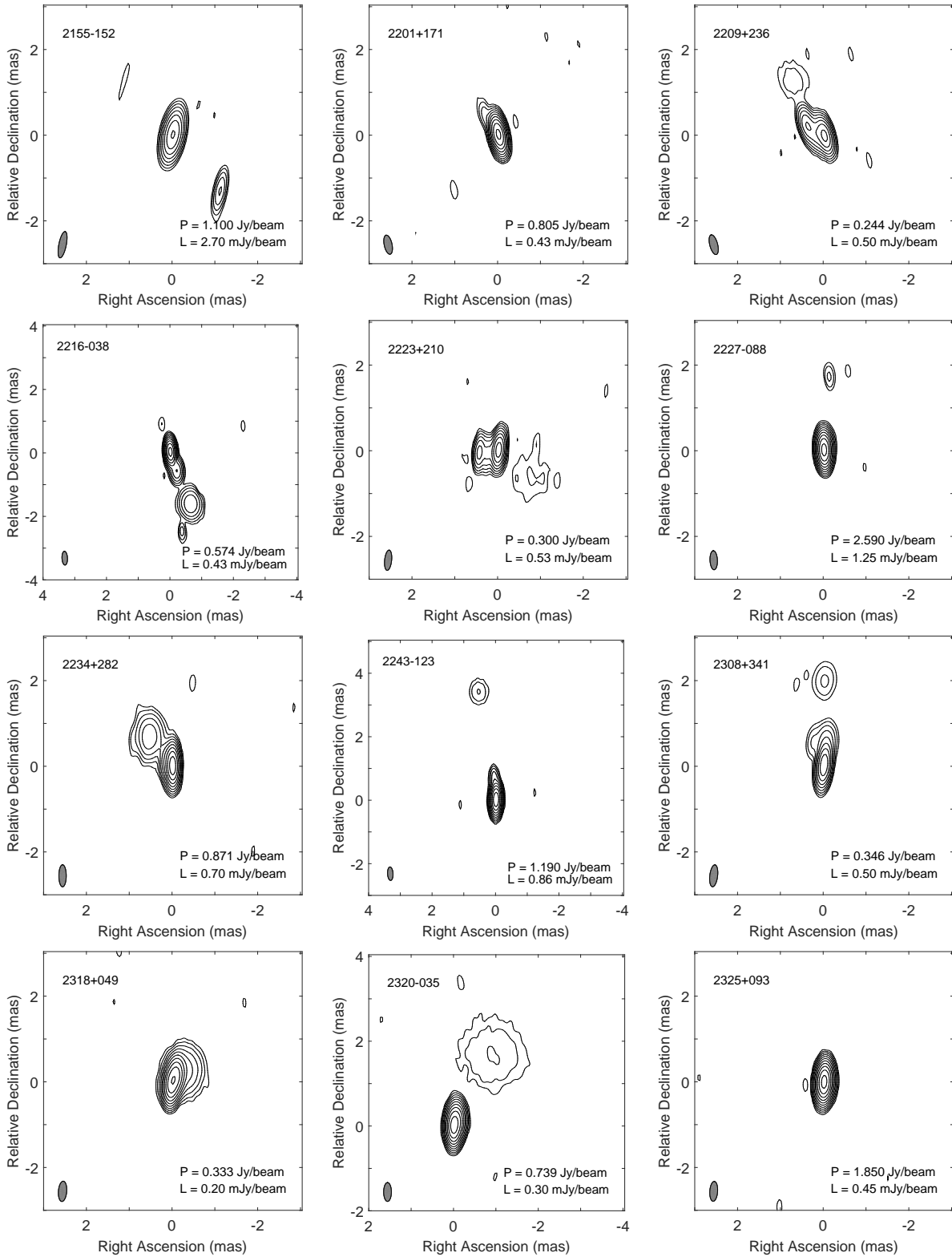


Fig. 11.— VLBA images — Continued

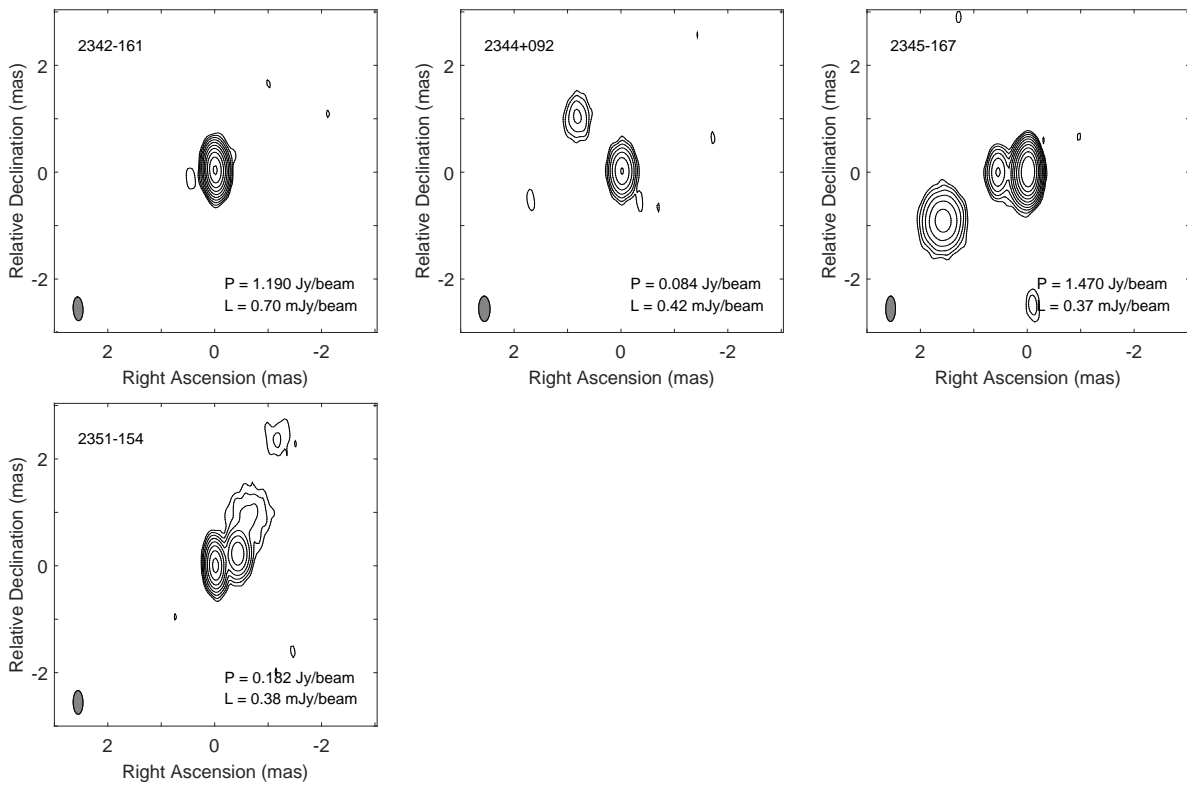


Fig. 12.— VLBA images — Continued

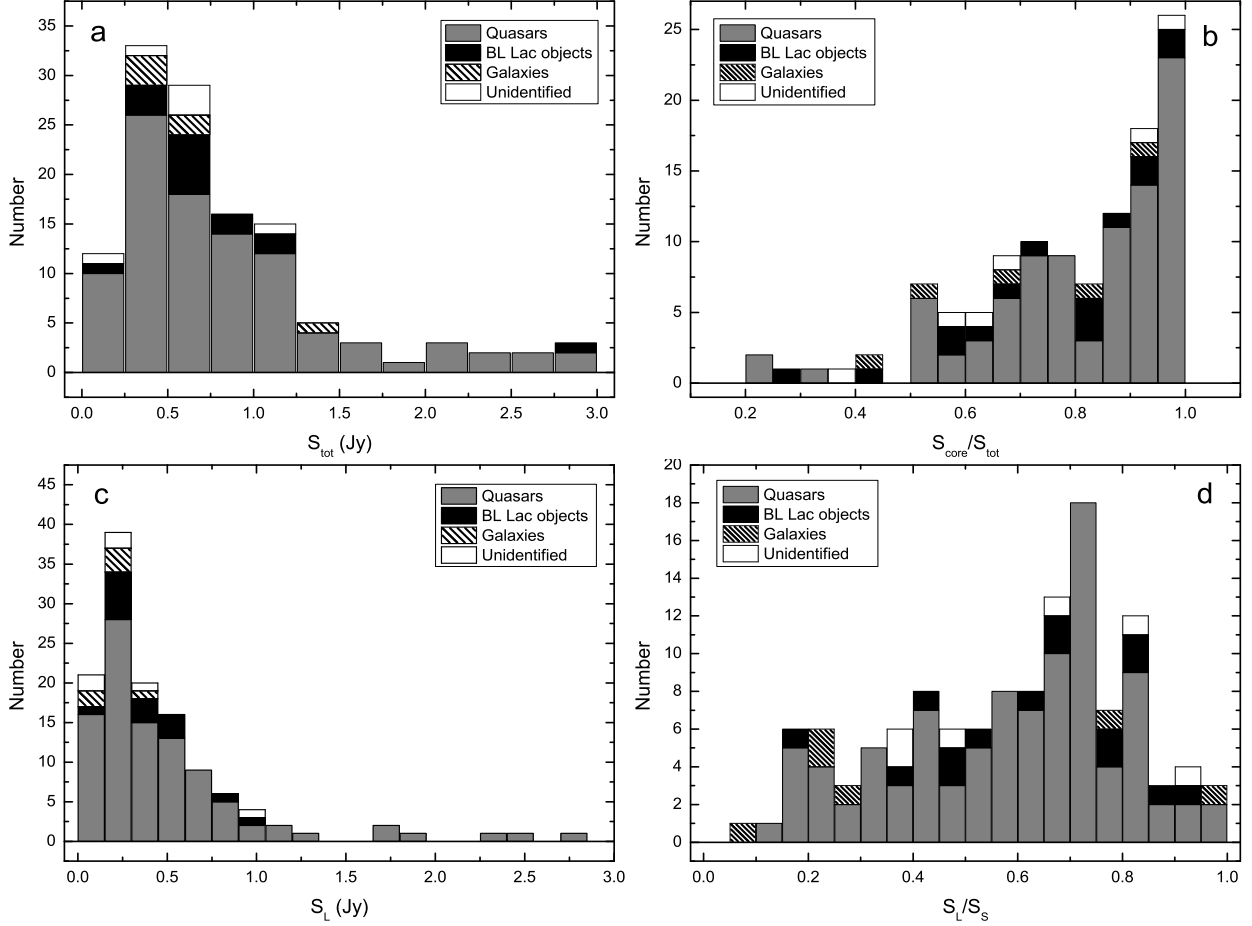


Fig. 13.— Histograms of the total flux density, S_{tot} (panel a), the compactness parameter on mas scales $S_{\text{core}}/S_{\text{tot}}$ (panel b), the correlated flux density on the longest baselines S_L (panel c), and the compactness parameter on sub-mas scales S_L/S_s (panel d).

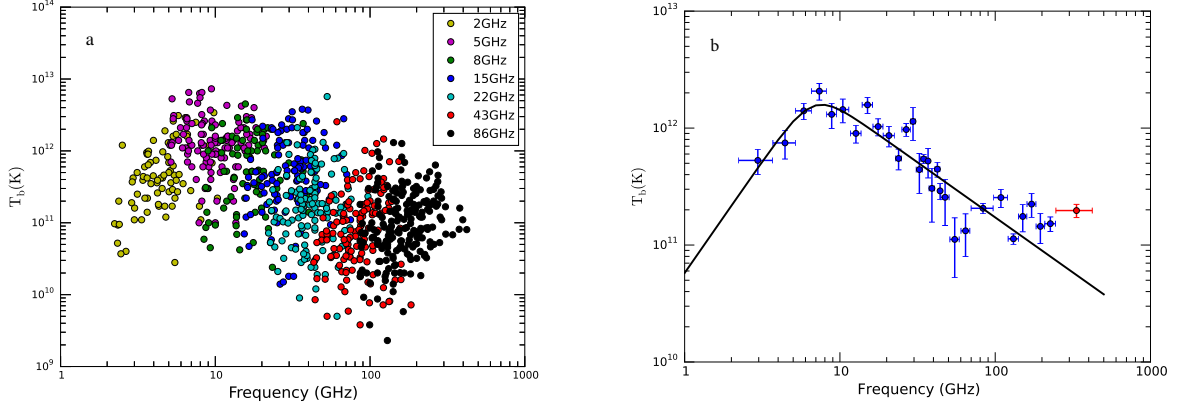


Fig. 14.— Distribution of core brightness temperature as a function of frequency (left panel) and the best fit of the relationship (right panel). Coloured symbols represent core brightness temperatures measured at various observed frequencies: yellow (2 GHz, Pushkarev & Kovalev 2012), purple (5 GHz, Horiuchi et al. 2004), green (8 GHz, Pushkarev & Kovalev 2012), blue (15 GHz, Kovalev et al. 2005), cyan (22 GHz, Moellenbrock et al. 1996), red (43 GHz, Cheng et al. 2018, and this paper), black (86 GHz, Lee et al. 2008; Cheng et al. 2018; Nair et al. 2019). The frequencies have been converted into the source rest frame. The fitting in the right panel is represented with a broken power-law function as described in Sect. 4.2.

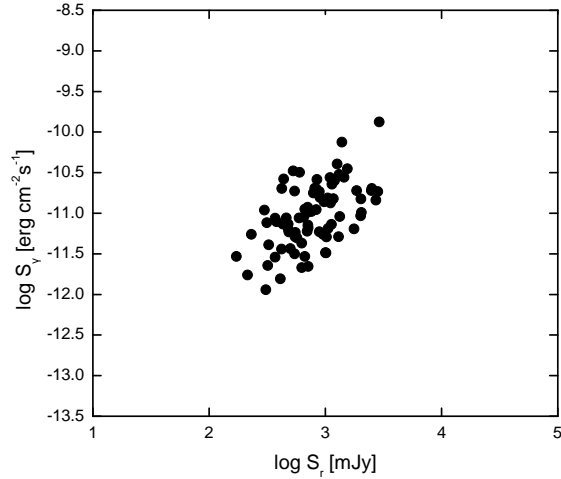


Fig. 15.— Flux density correlations between radio 43 GHz and γ -ray bands. The correlation coefficient is 0.550. The error bars are omitted for the clarity of the plot.